TUDelft

Delft University of Technology

A damaging block-based model for the analysis of the cyclic behaviour of full-scale masonry structures

D'Altri, Antonio Maria; Messali, Francesco; Rots, Jan; Castellazzi, Giovanni; de Miranda, Stefano

Important note
To cite this publication, please use the final published version (if applicable).
Please check the document version above.

A damaging block-based model for the analysis of the cyclic behaviour of full-scale masonry structures

Antonio Maria D'Altri[1]*, Francesco Messali[2], Jan Rots[2], Giovanni Castellazzi[1], Stefano de Miranda[1]

[1] Department of Civil, Chemical, Environmental, and Materials Engineering (DICAM), University of Bologna, Viale del Risorgimento 2, Bologna 40136, Italy

[2] Faculty of Civil Engineering and Geosciences, Delft University of Technology, Delft, The Netherlands

*corresponding author

ABSTRACT

In this paper, a damaging block-based model is proposed for the numerical analysis of the cyclic behaviour of full-scale masonry structures. Solid 3D finite elements governed by a plastic-damage constitutive law in tension and compression are used to model the blocks, while a cohesive-frictional contact-based formulation is developed to simulate their cyclic interaction. The use of tests on small-scale specimens to calibrate the mechanical properties of the numerical model is presented and discussed. The tests belong to a comprehensive experimental campaign performed on calcium silicate brick masonry. The calibrated models are used to simulate in-plane and out-of-plane cyclic tests on masonry walls made of the same material, as well as a quasi-static cyclic pushover test on a full-scale terraced masonry house. The efficiency, the potentialities and the accuracy of the model here proposed are shown and discussed. The capability of explicitly representing structural details (e.g. running bonds) and any in-plane and through-thickness texture of masonry, which appears essential to study the response of masonry structures, is guaranteed by the block-based modelling approach. A good agreement between the numerical results and the experimental outcomes is observed. This allows to validate the model in the cyclic response as well as the strategy proposed for its mechanical characterization.

Keywords: Unreinforced masonry; Cohesive behaviour; Cyclic behaviour; Earthquake; Terraced house; Masonry constitutive model

Nomenclature		
		cohesion of the contact shear response
d		degradation damage variable for the plastic-damage model
D		scalar damage variable for the contact behaviour
d_c		compressive scalar damage variable the plastic-damage model
d_t		tensile scalar damage variable the plastic-damage model
E		Young's modulus of the material
E_0		E_0 is the initial Young's modulus of the material
$\boldsymbol{E_0}$		initial undamaged elastic stiffness tensor
F		yielding surface
f_{b0}		biaxial initial compressive strength
f_{c0}		uniaxial initial compressive strength
f_s		contact shear strength
f_t		contact tensile strength
f_{t0}		initial uniaxial tensile strength
g_c		dissipated energy density in compression
g_t		dissipated energy density in tension
G		shear modulus
G_c		fracture energy in compression
G_t		fracture energy in tension
h		localization zone size (characteristic length)
I_1		first invariant of the stress tensor

J_2	second invariant of the stress deviator
J	Jacobian of the transformation
k_c	hardening variable in compression
k_t	hardening variable in tension
K_{nn}	contact cohesive stiffness in normal direction
K_{ss}	contact cohesive stiffness in shear direction
$r(\widehat{\overline{\sigma}})$	weight factor
s_c, s_t	functions of the stress state
$\tan\phi$	initial friction of the contact shear response
u	contact normal displacement
u_0	separation at the limit of the linear elastic behaviour in tension
u_k	ultimate separation of the cohesive behaviour
u_{MAX}	maximum separation ever experienced by the contact point
V_e	area of the finite element
w_η, w_ξ, w_ρ	weight factors
α	dimensionless constant
α_h	modification factor depending on the typology of the finite element
$\beta(\boldsymbol{k})$	function of the hardening variables
γ	dimensionless constant
δ	contact tangential slip
δ_0	slip at the limit of the linear elastic behaviour in shear
δ_k	ultimate slip of the cohesive behaviour
δ_{MAX}	maximum slip ever experienced by the contact point
$\boldsymbol{\varepsilon}$	strain tensor
ε_c	uniaxial compressive strain
ε_t	uniaxial tensile strain
$\boldsymbol{\varepsilon^p}$	plastic part of the strain tensor
$\dot{\boldsymbol{\varepsilon}}^p$	plastic strain rate tensor
$\widehat{\dot{\boldsymbol{\varepsilon}}^p}$	matrix which collects the eigenvalues of the plastic strain rate tensor
ε_c^p	uniaxial compressive plastic strain
ε_t^p	uniaxial tensile plastic strain
ϵ	smoothing constant
ζ	brittleness parameter in tension
$\dot{\lambda}$	plastic multiplier
μ	residual friction
ν	Poisson's coefficient
ξ	brittleness parameter in shear
ρ	dimensionless constant
σ	contact normal stress
$\boldsymbol{\sigma}$	stress tensor
$\overline{\boldsymbol{\sigma}}$	effective stress tensor
$\widehat{\overline{\boldsymbol{\sigma}}}$	matrix which collects the eigenvalues of the effective stress tensor
σ_c	uniaxial compression
$\overline{\sigma}_{MAX}$	algebraically maximum principal stress in the effective-stress space
σ_t	uniaxial tension
$\sigma_{uniaxial}$	uniaxial stress
ς_c	uniaxial compressive strength function
$\overline{\varsigma_c}$	uniaxial compressive strength function in the effective-stress response
ς_t	uniaxial tensile strength function
$\overline{\varsigma_t}$	uniaxial tensile strength function in the effective-stress response
τ	contact shear stress
τ_1, τ_2	shear stress components along two orthogonal directions in the plane of the contacting surface
Φ	plastic potential
ψ	dilatancy angle of the quasi-brittle material

1   Introduction

A large part of the existing buildings in Europe is composed of masonry structures. On the one hand, monumental masonry structures represent fascinating examples of historic architecture [1]. On the other hand, ordinary masonry buildings constitute one of the most widespread building typologies [2]. However, masonry constructions are sensibly vulnerable to earthquake actions. Even light seismic events can induce considerable damage to masonry buildings. This is the case, for example, of the terraced masonry houses in the Groningen region (the Netherlands) [3], which, in recent years, has been subjected to earthquakes due to gas extraction in the soil.

Predictions of the response of masonry structures against extraordinary loads (e.g. seismic loads) can be performed by means of numerical approaches, which could also evaluate the main weaknesses of these structures. However, the mechanical behaviour of masonry is very complex and highly nonlinear, due to the composite nature and the heterogeneity of masonry (made of blocks usually bonded with mortar). Therefore, the definition of reliable numerical models for masonry assemblages is a very challenging task and an on-going process in the scientific research [4].

Computational strategies for masonry structures can be classified in: (i) pier-spandrels models, (ii) continuum homogeneous models and (iii) block-based models. Pier-spandrels models represent the structure by means of macroscopic elements which model the behaviour of piers, spandrels and joint between them [5]. Conversely, continuum homogeneous models represent masonry by means of a continuum discretization of the geometry. The definition of the constitutive law of the material can be obtained through a direct approach [6, 7, 8] or a multi-scale approach [9, 10, 11]. Finally, block-based models account for the texture of masonry by an explicit and separated representation of each block of the structure. The mechanical behaviour of the blocks is usually considered rigid or linear elastic and the interaction between them is accounted for through several formulations: interface elements [12, 13, 14, 15, 16, 17], strong discontinuity approaches [18, 19], finite element (FE) limit analysis approaches [20, 21, 22, 23], and contact-based formulations [24, 25, 26]. To account for the cracking of masonry blocks, several approaches employed interface elements or disconnections along the central plane of the blocks.

Generally, this latter category of models can capture the complex patterns of cracks which characterize the evolution of the damage in masonry with more accuracy, reproducing the main aspects of the nonlinear response such as, for example, the relative sliding of blocks. Furthermore, these models can represent the actual texture of a structure and, therefore, can accurately represent complex structural details (e.g. running bonds and toothing between orthogonal walls), which can be substantial in the structural response under horizontal loading [27]. Particularly, the use of solid 3D blocks permits to account for in-plane and out-of-plane behaviours at the same time.

In order to better represent the response of masonry structures undergoing earthquakes, the cyclic behaviour of masonry should be accounted for. However, only few of the cited papers take it into consideration. Indeed, more aspects (e.g. stiffness degradation, residual displacements and hysteresis) have to be accounted for to model the cyclic behaviour of masonry. To this aim, in [28] a cyclic 2D model entirely based on multi-surface plasticity has been developed and, in [29], a 3D softening plasticity model has been implemented to represent the stiffness degradation in the normal direction in a simplified way.

More effective approaches for the definition of the cyclic cohesive interface behaviour are based on the coupling of plasticity and damage. In this framework, a 2D model where the evolution of the inelastic strains is coupled to the evolution of a damage variable has been developed and validated in [30]. Furthermore, numerical approaches based on micro-mechanical hypotheses of damage mechanics, which employ a decomposition of stresses in two components to account for the damaged and undamaged part of the interface, have been presented in [31, 32]. Inelastic strains are associated with the former stress component to represent the crack opening and/or the slip in the damaged part of the interface.

More recently, in [33] the applied element method has been utilized to model calcium silicate brick masonry subjected to in-plane cycling loading, whereas in [34] a constitutive model for the masonry joint interfaces under cyclic loading has been proposed. This model is based upon the combination of plasticity and damage,

using a multi-surface yield criterion in the stress domain which governs the development of permanent plastic strains.

Very recently, a 3D detailed micro-model to analyse the mechanical response of masonry panels under in-plane and out-of-plane loading conditions has been proposed by part of the Authors in [35]. This modelling approach is characterized by textured units, consisting of one brick and few mortar layers, represented by 3D nonlinear solid finite elements. Textured units are assembled by means of zero-thickness rigid-cohesive-frictional interfaces based on the contact penalty method. Although this latter approach represents an advanced model for the mechanical analysis of masonry, it has been investigated and validated in the monotonic regime only.

In this paper, following an approach akin to the one proposed in [35] and aiming to extend it to the cyclic behaviour, a novel damaging block-based model is proposed for the numerical analysis of the cyclic behaviour of full-scale masonry structures. Solid 3D finite elements governed by a plastic-damage constitutive law in tension and compression are used to model the blocks, accounting for masonry crushing and cracking of the blocks. A cohesive-frictional contact-based formulation is developed to simulate their interaction, accounting for the sliding and the separation of the blocks also in the cyclic regime. In particular, a Mohr-Coulomb failure surface with tension cut-off governs the contact behaviour.

This novel modelling approach can, in fact, be fully characterized by the properties obtained through monotonic tests on small-scale masonry assemblages. A strategy for the comprehensive mechanical characterization of the mechanical properties of the numerical model from these small-scale experiments is discussed in the paper. In particular, an experimental campaign on calcium silicate masonry small-scale specimens is used to calibrate the mechanical properties of the model. These mechanical properties are used to simulate in-plane and out-of-plane cyclic tests on masonry walls made of the same material, as well as a cyclic pushover test on a full-scale terraced masonry house. The efficiency of the contact-based formulation and the potentialities and the accuracy of the model herein proposed are discussed.

The paper is organized as follows. Section 2 illustrates the proposed damaging block-based model and the strategy for its mechanical characterization from small-scale tests on masonry. Section 3 briefly describes the experimental campaign on calcium silicate masonry used as reference in the paper. Section 4 describes the calibration of the mechanical properties from the small-scale tests presented in Section 3. Section 5 collects experimental-numerical comparisons and their discussion for the in-plane and out-of-plane behaviour of masonry walls, as well as for the cyclic pushover test on a terraced masonry house. Finally, Section 6 highlights the conclusions of this research work.

2   Damaging block-based modelling

The novel modelling approach herein proposed for the analysis of the cyclic behaviour of masonry structures consists of a block-based model. In this model, the interaction between adjacent blocks is formulated in a contact-based framework (Fig. 1) accounting for cohesion and friction, whereas the blocks follow a continuum plastic-damage constitutive law [36] both in tension and compression. As the mortar layers are not explicitly modelled, the use of expanded blocks is adopted, as commonly employed in block-based models [12, 14]. The model is implemented in Abaqus [37], a general-purpose FE software.

The adopted contact formulation conceives contact pairs composed of one slave face and one master face, following the traditional node-against-surface approach [38] (Fig. 1). In particular, the nodes of the slave face contact the surface of the master face (Fig. 1). Therefore, contact is enforced at discrete points, which are the nodes of the slave face. After the assembly of the blocks, the contact pairs between adjacent blocks are defined by means of fully automatic contact detection algorithms [37]. A finite-sliding formulation, which allows for arbitrary separation, sliding, and rotation of the surfaces, is adopted [37]. The cohesive contact behaviour is governed by an ad-hoc modification of the standard surface-based contact behaviour available in Abaqus [37]. In this context, an automatic subroutine ad-hoc written by the authors is implemented to reproduce a Mohr-Coulomb failure surface with tension cut-off.

The sliding between blocks is conceived without a dilatant behaviour, whereas dilatancy is considered in the 3D nonlinear FEs used for the blocks, in the framework of nonassociated plasticity [36]. Indeed, although the role of dilatancy in the mechanical behaviour of masonry is still under investigation [39, 40], the experimental tests collected in [41] show that dilatancy is considerably influenced by the failure type, i.e. higher dilatancy is recorded when the crack crosses mortar and/or blocks rather than that recorded when the bond between block and mortar undergoes failure.

The formulation of the proposed model allows for a direct setting of the mechanical parameters from small-scale experimental tests on masonry specimens. The main idea at the base of this setting is that the properties of the cohesive-frictional behaviour between blocks are based on brick-mortar bond tests (tensile failure and shear sliding), whereas the properties of the block 3D FEs are based on tests on masonry wallets and on tests on single bricks.

In the following, the description of the contact mechanical behaviour, the block nonlinear behaviour, as well as the strategy suggested for the mechanical characterization of the model mechanical properties from small-scale tests on masonry are illustrated.
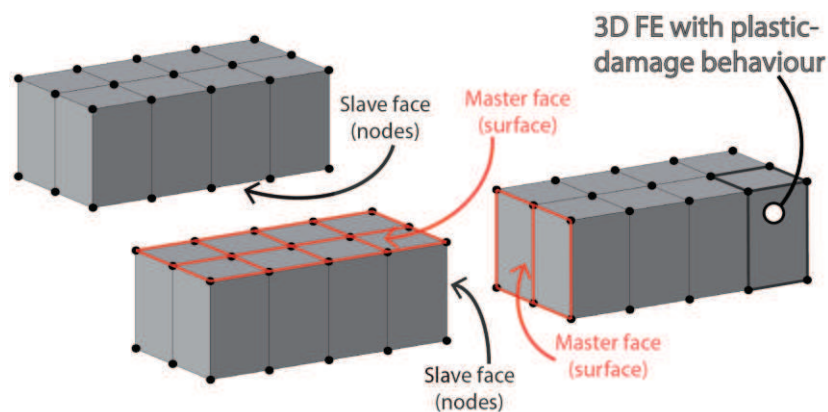

Fig. 1 – Node-against-surface contact approach adopted in the damaging block-based modelling.

2.1 Contact mechanical behaviour

In the normal direction, the contact stress σ is computed by means of a pressure-overclosure relationship in compression and a linear elastic relationship in tension:

$$\sigma = \begin{cases} \text{Pressure} - \text{overclosure relationship}, & u < 0 \\ K_{nn}u, & u \geq 0 \end{cases} \tag{1}$$

where K_{nn} is the cohesive stiffness in normal direction and u is the normal displacement (separation). The pressure-overclosure relationship represents the approach used to enforce the contact constraints. Several numerical strategies have been proposed to deal with the contact constraints [42]. The most common approaches are Lagrange multiplier methods and penalty methods. Lagrange multiplier methods introduce additional multipliers to enforce directly and exactly the contact constraint, whereas penalty methods avoid the need for additional variables by introducing an approximation of the constraint condition. In this paper, the Lagrange multiplier approach implemented in Abaqus (hard contact) is adopted [37]. Relationship (1) is assumed to be valid for tensile stresses until the tensile strength f_t of the contact behaviour is reached, whereas it is always valid in the compressive regime.

In the shear direction, the tangential slip δ is linearly related to the contact shear stress τ with the relation:

$$\tau = K_{ss}\delta, \tag{2}$$

where K_{ss} is the cohesive stiffness in shear. This relation is valid until the contact shear stress equals the shear strength f_s. The shear strength f_s is assumed to be dependent on the contact stress:

$$f_s(\sigma) = -\tan\phi\,\sigma + c, \tag{3}$$

where c is the cohesion and $\tan\phi$ is the initial friction of the shear response.

Therefore, contact failure is supposed when the contact stresses at a point intersects a Mohr-Coulomb failure surface with tension cut-off. This criterion can be expressed as:

$$\max\left\{\frac{\langle\sigma\rangle}{f_t}, \frac{\tau}{f_s(\sigma)}\right\} = 1, \tag{4}$$

where the symbol $\langle x \rangle = (|x| + x)/2$ denotes the Macaulay bracket function. The Macaulay brackets are used to signify that a purely compressive stress state does not induce contact failure. A sketch of the failure surface adopted for the contact behaviour is shown in Fig. 2. Once contact failure is reached, cohesive behaviour in tension and cohesive-frictional behaviour in shear is activated.
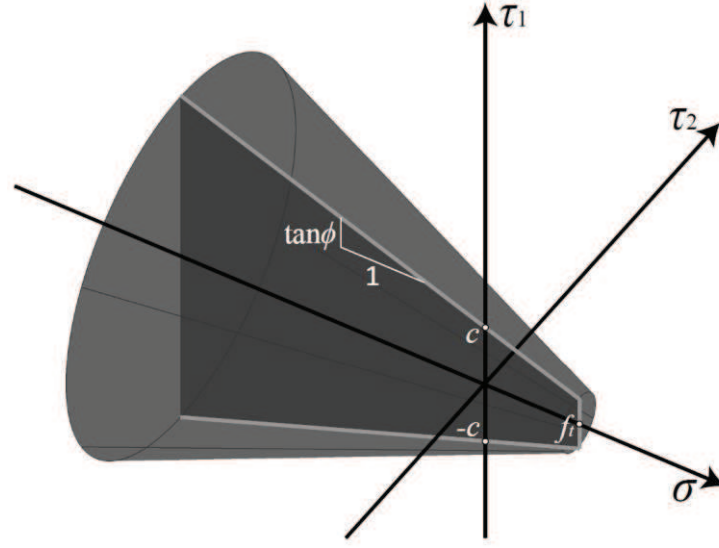
Fig. 2 – Morh-Coulomb failure surface with tension cut-off (τ_1 and τ_2 are the shear stress components along two orthogonal directions in the plane of the contacting surface).

The maximum value of the stress in the post-peak regime, in a contact point, is described in tension by the relationship:

$$\sigma = \begin{cases} (1-D)f_t, & u_0 < u < u_k \\ 0, & u \geq u_k \end{cases}, \tag{5}$$

and in shear by the relationship:

$$\tau = \begin{cases} (1-D)f_s(\sigma) + D\mu\langle-\sigma\rangle, & \delta_0 < \delta < \delta_k \\ \mu\langle-\sigma\rangle, & \delta \geq \delta_k \end{cases}, \tag{6}$$

where the degradation scalar variable D is defined as:

$$D = \max \begin{cases} 1 - \dfrac{u_0}{u_{MAX}}\left(1 - \dfrac{1 - e^{-\zeta\frac{u_{MAX}-u_0}{u_k-u_0}}}{1 - e^{-\zeta}}\right) \\ \\ 1 - \dfrac{\delta_0}{\delta_{MAX}}\left(1 - \dfrac{1 - e^{-\xi\frac{\delta_{MAX}-\delta_0}{\delta_k-\delta_0}}}{1 - e^{-\xi}}\right) \end{cases}, \tag{7}$$

being μ the residual friction, u_0 and δ_0 the separation and the slip at the limit of the linear elastic behaviour in tension and shear, respectively, u_{MAX} and δ_{MAX} the maximum separation and the maximum slip ever experienced by the contact point, respectively, u_k and δ_k the ultimate separation and the ultimate slip of the cohesive behaviour, respectively, ζ and ξ non-dimensional brittleness parameters in tension and shear, respectively.

From equations (5), (6) and (7) it appears clear that the cohesive behaviour in tension and shear is governed by the same degradation scalar variable D. Indeed, the damage evolution in tension and shear are fully coupled, i.e. the degradation of cohesion in tension degrades the cohesion in shear and vice versa.

Fig. 3 and Fig. 4 show the contact normal and shear cyclic behaviour, respectively. The monotonic behaviour is depicted by means of black thick lines.

Dealing with the tensile contact behaviour (Fig. 3), if a degraded contact point with $0 < D < 1$ undergoes unloading, the unloading path will be characterized by a linear branch with a degraded stiffness $(1 - D)K_{nn}$ until the stress state reach compression. In the compression regime, the behaviour is fully governed by the pressure-overclosure relationship adopted, which is completely independent by the state of degradation of the cohesion.

As can be noted in Fig. 4, the contact shear cyclic behaviour appears more complex than the normal one, as it is also governed by friction. If a degraded contact point $(0 < D < 1)$, e.g. point A in Fig. 4, undergoes unloading, the unloading path will be characterized by a bi-linear branch. The first segment will be defined by the initial stiffness K_{ss} and by a stress drop equal to two times the maximum frictional contribution, i.e. $2\mu\langle-\sigma\rangle$. Therefore, the length of the first segment, e.g. AB in Fig. 4, will be equal to $\overline{AB} = 2\mu\langle-\sigma\rangle\sqrt{1 + \frac{1}{K_{ss}^2}}$.

The second segment, conversely, will be characterized by a degraded stiffness $(1 - D)K_{ss}$ until the reaching of point C (Fig. 4), which represents the specular point of A in Fig. 4. From this point forward, the cohesive exponential behaviour is re-established, and the contact point further degrades (for example, moving from point C to point D in Fig. 4). If a fully degraded contact point $(D = 1)$, e.g. point G in Fig. 4, undergoes unloading, the unloading path will be characterized by a bi-linear branch, in which the first segment will be defined by the initial stiffness K_{ss} and by a stress drop equal $2\mu\langle-\sigma\rangle$, whereas the second segment will be characterized by an horizontal line, purely governed by friction.

The contact shear cyclic behaviour proposed has been found to be consistent with the experimental results obtained by Atkinson et al. [43] on small-scale masonry samples, as well as with the numerical results found by Gambarotta & Lagomarsino [30], as shown in Fig. 5.
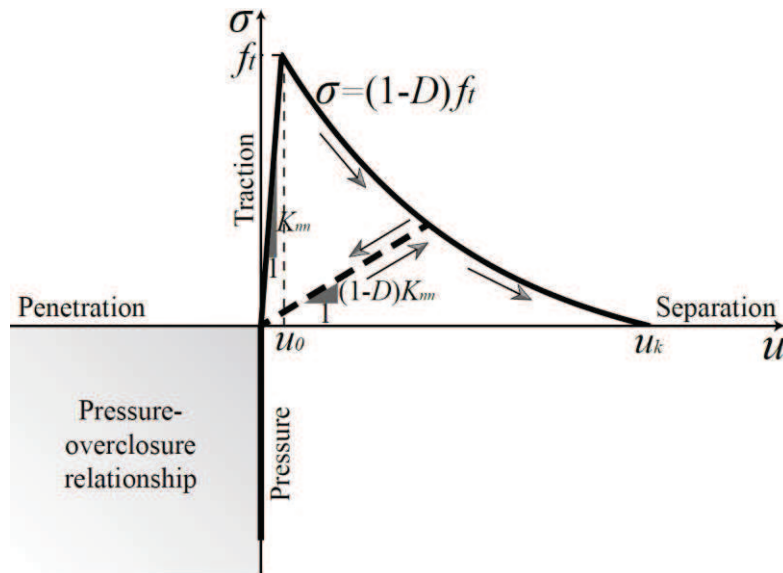

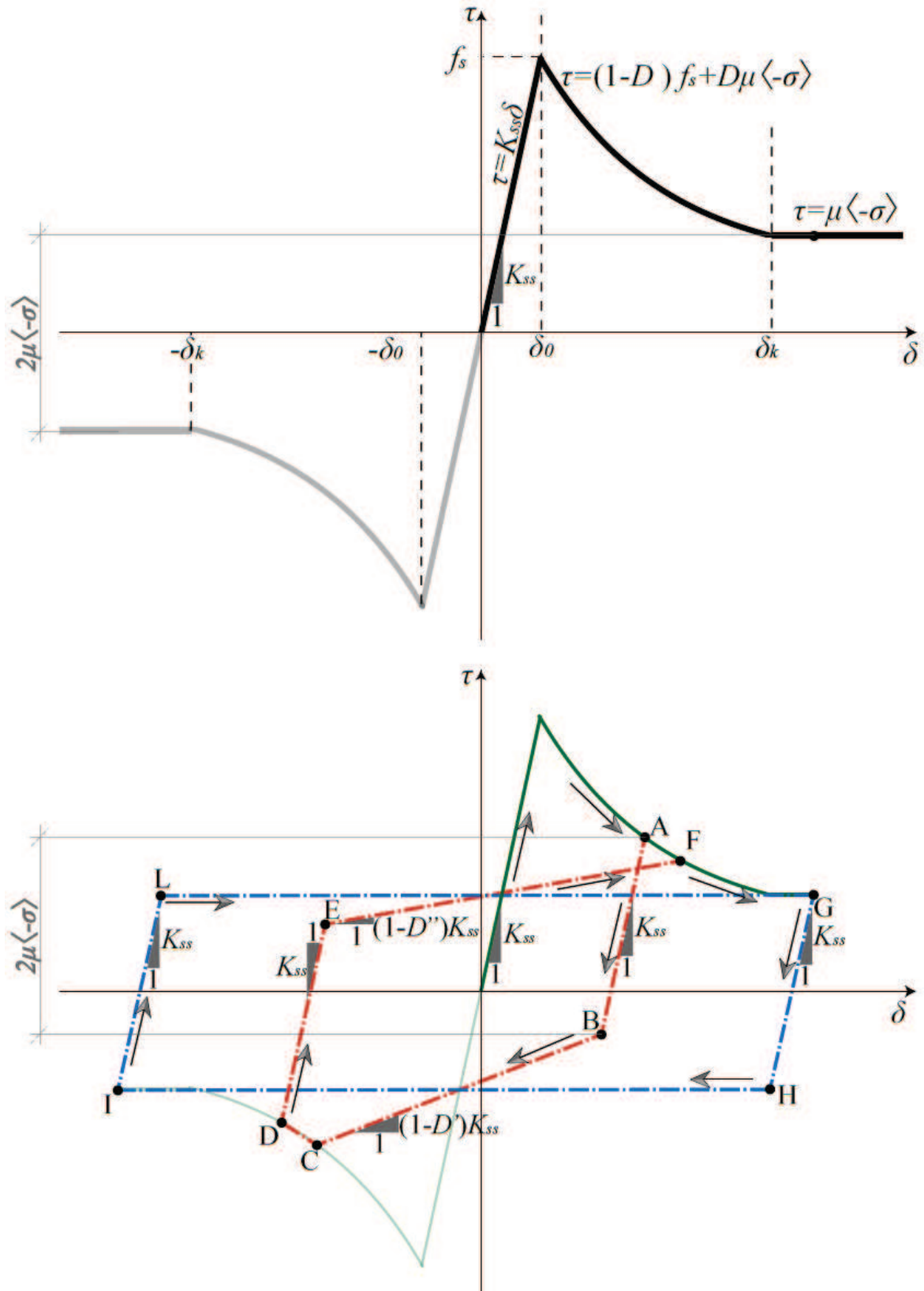
Fig. 3 – Contact normal cyclic behaviour.

Fig. 4 – Contact shear cyclic behaviour. Two unloading-reloading paths are indicated: ABCDEF in the shear softening stage, GHIL in the final shear friction stage. D' and D'' are the values assumed by the degradation scalar damage variable D when reaching the point A and the point D, respectively.
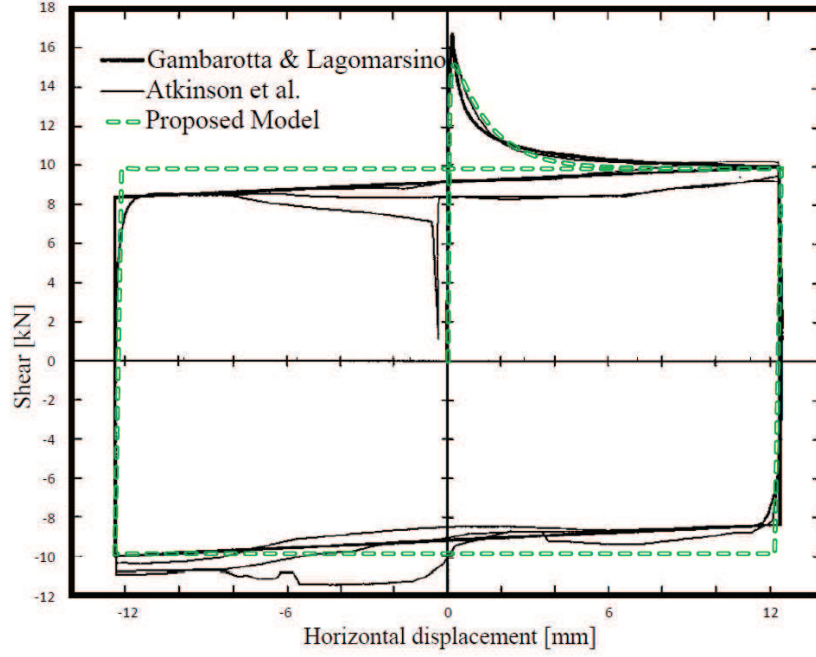
Fig. 5 – Cyclic shear behaviour of masonry joints: Comparison between experimental tests (old bricks specimen in [43]) and numerical response.

2.2 Block nonlinear behaviour

The isotropic plastic-damage nonlinear behaviour based on the constitutive model developed by Lee and Fenves [36] for quasi-brittle materials is assumed for blocks. In the following, the main characteristics of the model are recalled. For the reader's convenience, a summary of the model equations, accounting for the role of the parameters involved, is given in the Appendix.

Two independent scalar damage variables are assumed for the tensile response $(0 \leq d_t < 1)$ and for the compressive response $(0 \leq d_c < 1)$. Consequently, the stress-strain relations in uniaxial tension, σ_t, and compression, σ_c, are:

$$\sigma_t = (1 - d_t)E_0\big(\varepsilon_t - \varepsilon_t^p\big), \qquad \sigma_c = (1 - d_c)E_0\big(\varepsilon_c - \varepsilon_c^p\big), \qquad (8)$$

where E_0 is the initial Young's modulus of the material, ε_t and ε_c are the uniaxial tensile and compressive strains, and ε_t^p and ε_c^p are the uniaxial tensile and compressive plastic strains (Fig. 6). In particular, the curves shown in Fig. 6 characterize the main input data of the continuum model.

In addition, a nonassociative flow rule is considered to govern the dilatancy and to define the plastic strain rate. A flow rule obtained by a Drucker-Prager type plastic potential is considered. Particularly, the flow rule is controlled by the dilatancy angle ψ, generally assumed equal to 10° in agreement with physical evidences [44] and previous computational approaches [45, 46], and a smoothing constant ϵ typically assumed equal to 0.1 [45].

Finally, a multiple-hardening Drucker-Prager type surface is adopted as yield surface. This surface is governed by the ratio f_{b0}/f_{c0} between the biaxial initial compressive strength f_{b0} and the uniaxial initial compressive strength f_{c0} and a constant ρ, which represents the ratio of the second stress invariant on the tensile meridian to that on the compressive meridian at initial yield. Generally, $f_{b0}/f_{c0} = 1.16$ and $\rho = 2/3$ for quasi-brittle materials, such as masonry [47]. The general parameters adopted for blocks are collected in Table 1.

Table 1. General parameters for the blocks.

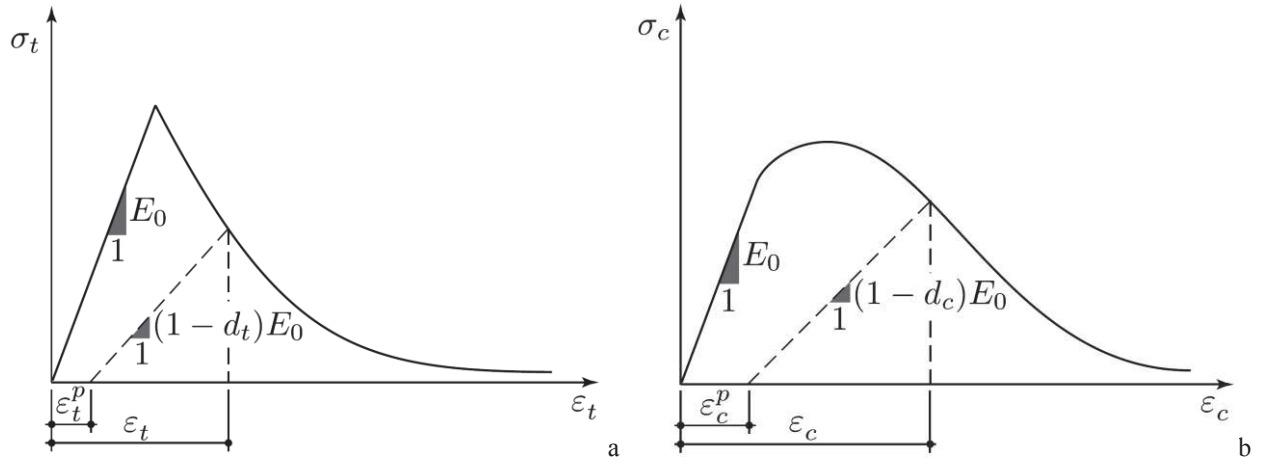| ϵ	ψ	f_{b0}/f_{c0}	ρ
0.1	10°	1.16	2/3

Fig. 6 – Plastic-damaging behaviour of blocks: a) tensile and b) compression uniaxial nonlinear curves.

2.3   Mechanical characterization of the model from small-scale experimental test

The proposed numerical model allows for a direct and easy setting of the mechanical parameters. The strategy that can be used for the mechanical characterization of the model based on monotonic small-scale experimental tests on masonry wallets and components is summarised in Fig. 7. The main idea at the base of this setting is that the properties of the contact cohesive-frictional behaviour between blocks are based on brick-mortar bond tests, whereas the properties of the block 3D FEs are based on tests on masonry wallets and blocks.
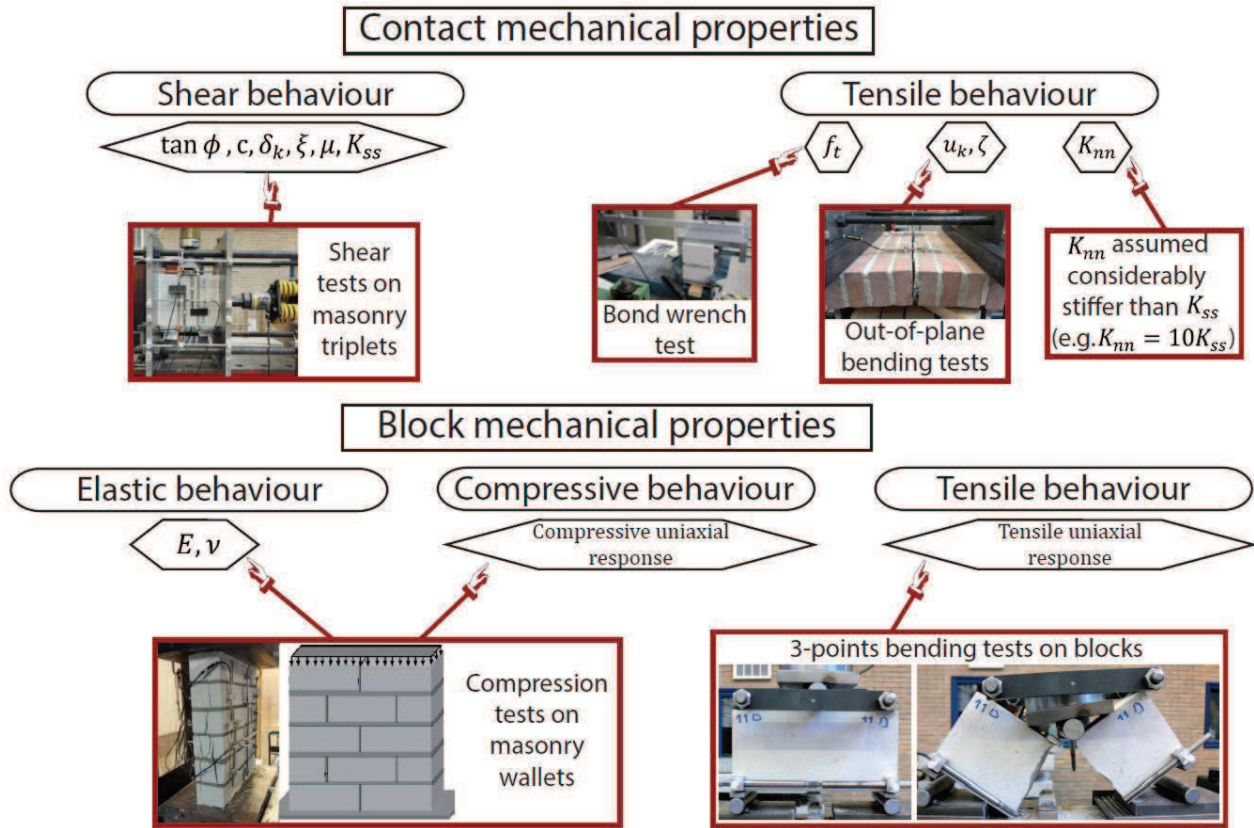

Fig. 7 – Strategy for the mechanical characterization of the model from small-scale experimental tests on masonry components and assemblages.

The contact shear behaviour can be completely defined by shear tests on masonry triplets (Fig. 7). The output of experimental tests on triplets (at least with 3 different levels of pre-compression) in terms of cohesion (c), initial friction ($\tan\phi$) and residual friction (μ) can be directly used as mechanical properties in the numerical model. Moreover, the ultimate slip of the cohesive behaviour (δ_k) and the brittleness parameter ξ can be calibrated in order to better fit the post peak behaviour of the tests, as well as to better approximate the Mode II fracture energy. Finally, the shear cohesive stiffness (K_{ss}) can be determined by fitting the initial linear branch of the shear-slip curve. Indeed, in the simulation of these tests, the deformability of the blocks plays a marginal role.

The contact normal characterization needs even less parameters (Fig. 7). As a matter of fact, the compressive contact behaviour does not need any parameter to be characterized. The tensile cohesive behaviour can be characterized by bond wrench tests, in terms of tensile strength (f_t), and out-of-plane bending tests which can be used to characterize the Mode I fracture energy and, also, can be used to verify the tensile strength measured by wrench tests. From the Mode I fracture energy, the ultimate separation of the cohesive behaviour (u_k) and the brittleness parameter ζ can be calibrated. The cohesive stiffness in the tensile direction K_{nn} represents a further component of deformability in the normal direction, which acts only in the tensile regime. Although the Young's modulus of masonry in compression could be, in theory, different from the one in tension, no deep experimental investigation has been conducted on this topic. Therefore, the use of a stiff value of K_{nn}, considerably stiffer than K_{ss} (e.g. $K_{nn} = 10 K_{ss}$), is suggested.

Dealing with the block mechanical properties, the continuum isotropic elastic properties as well as the compressive and tensile uniaxial nonlinear curves depicted in Fig. 6 need to be characterized (Fig. 7). As in the compressive regime the contact formulation does not account for any failure as well as any deformability, the compression tests on masonry wallets can be used to characterize the block elastic properties, in terms of Young's modulus E and Poisson's coefficient ν, as well as the compressive nonlinear behaviour of the blocks. Therefore, the elastic and compressive responses of blocks is related to masonry properties. Conversely, the tensile nonlinear behaviour of the blocks is deduced from tests on blocks (e.g. 3-points bending tests, see Fig. 7), and, therefore, is related to a block property.

As one can note, the proposed numerical model shows, beyond the deformability of the continuum isotropic blocks, an additional deformability in the shear behaviour due to the cohesive stiffness K_{ss} (considering negligible the deformability due to K_{nn}). Therefore, dealing with a masonry panel, the overall shear modulus G evaluated with the proposed model will be lower than the one predicted with an isotropic continuum model with the same parameters E and ν. Of course, masonry is not an isotropic material and the relationship between the three elastic constants is, in general, not valid. Indeed, by using the measured values of E and ν in a continuum model, the value of G will be, in general, overestimated. In addition, the values of E and G generally adopted in beam-based piers-spandrels models [48] for the simulation of masonry structures often lead to values of ν which have no mechanical meaning (even $\nu > 0.5$). Therefore, the use of an additional deformability in the shear behaviour (governed by K_{ss}) allows the proposed model to overcome this limitation of continuum isotropic models. In particular, the authors experienced that the overall shear stiffness of masonry walls is generally gathered with a good accuracy by the proposed model utilizing the cohesive stiffness K_{ss} calibrated in triplet tests.

Finally, it has to be pointed out that the characterization of the mechanical parameters of the model can be fully described by monotonic tests on small-scale masonry specimens (and components), even if the model is suitable for cyclic simulations. This aspect constitutes a further appealing feature of the proposed model.

3   Experimental campaign

Extensive testing programs to characterize the behavior of masonry structures from a material to a structural level have been carried out at the laboratory of Delft University of Technology since 2014 [49]. At material level (small-scale tests), destructive laboratory tests were performed on both existing and replicated masonry specimens [50]. At structural level, several in-plane and out-of-plane tests on single piers have been performed [51]. Furthermore, the campaign comprehended also two quasi-static cyclic pushover tests on full-scale two-story high assembled structures [52]. All the tests considered have been conducted by using the same calcium silicate brick masonry.

3.1   *Small-scale tests*

Many small-scale tests on masonry samples (wallets, triplets, couplets) and on masonry components (brick and mortar) have been performed at the Stevin II laboratory at the Delft University of Technology [50, 53]. All the tests considered were performed on replicated calcium silicate brick masonry [53], made of 210x71x102 mm bricks. Standardized monotonic destructive material tests for the characterization of masonry have been conducted and the experimental set-ups and results were collected in [53]. Particularly, compression tests on masonry wallets, brick and mortar specimens, bending tests on masonry wallets, brick and mortar specimens, bond wrench tests on masonry couplets, and shear tests on masonry triplets have been performed.

3.2   *In-plane cyclic tests on masonry walls*

Seven 2.75 m high masonry walls made of calcium silicate brick masonry have been built and tested under in-plane cyclic loading. Two height/width aspect ratios (0.7 and 2.5) and two different configurations (i.e. cantilever and double clamped walls) were considered. In addition, different vertical pressure values have been initially applied to the walls. The used set-up provided a uniform vertical pressure and a horizontal imposed displacement on the top of the walls. A sketch of the set-up employed for the in-plane tests is shown in Fig. 8a. A quasi-static cyclic pushover test was performed on each wall in displacement control. Further details are collected in [51].

3.3   *Out-of-plane cyclic tests on masonry walls*

Four walls were also tested in the out-of-plane direction by applying a quasi-static cyclic loading using a system of airbags. Two different configurations (i.e. one-way and two-way spanning configurations) were considered. The tests were performed by employing a system of coupled airbags on both sides of the wall to apply a uniform pressure. The difference between the loads measured on both sides is the total out-of-plane load acting on the wall. A sketch of the set-up used in the tests (e.g. for the two-way spanning walls) is shown in Fig. 8b. The interested reader is referred to [51] for further details.
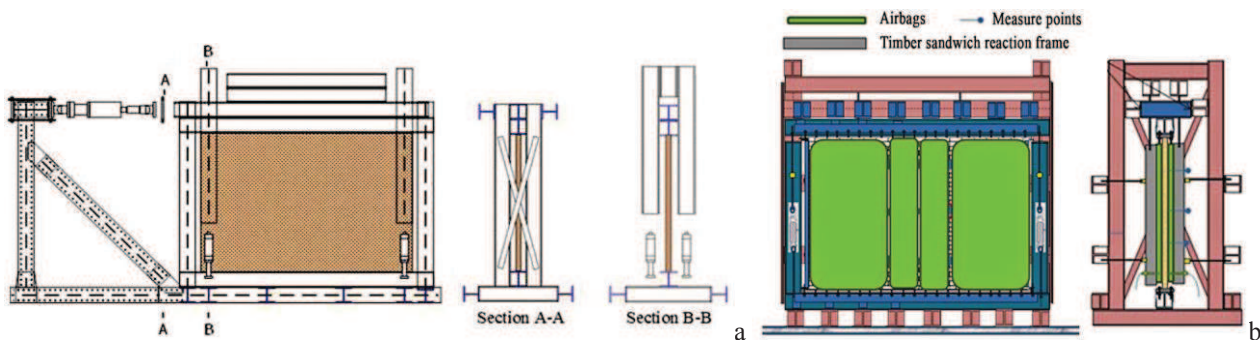

Fig. 8 – Sketch of the set-up used for the in-plane (a) and out-of-plane (b) tests on walls.

3.4 *Cyclic pushover test on a masonry full-scale terraced house*

The extensive experimental campaign conducted in Delft also included a terraced house typology, which was representative of the masonry constructions built in the Netherlands during the period 1960-1980. Two terraced houses (one made of calcium silicate bricks and the other of calcium silicate elements) were built and tested through a quasi-static cyclic pushover loading [49]. In this paper, reference to the calcium silicate brick masonry terraced house is made [52, 54]. The construction is characterised by the presence of large daylight opening in the facades. Consequently, the loadbearing structure is composed of very slender piers and long transversal walls (Fig. 9). The masonry bricks were laid using a stretcher bond and allowing for the interlocking of the bricks at the corners of the transversal walls and the piers (Fig. 9). Each floor consisted of two separated prefabricated concrete slabs spanning between the loadbearing transversal walls. A braced steel tower was built to apply the cyclic horizontal loading to the house. A quasi-static cyclic pushover test was performed on the terraced house. The test was performed in displacement control with the additional condition of maintaining equal the forces applied at the two floor levels through four actuators (two per each floor). For the reader convenience, reference to [52, 54] is made for further details.
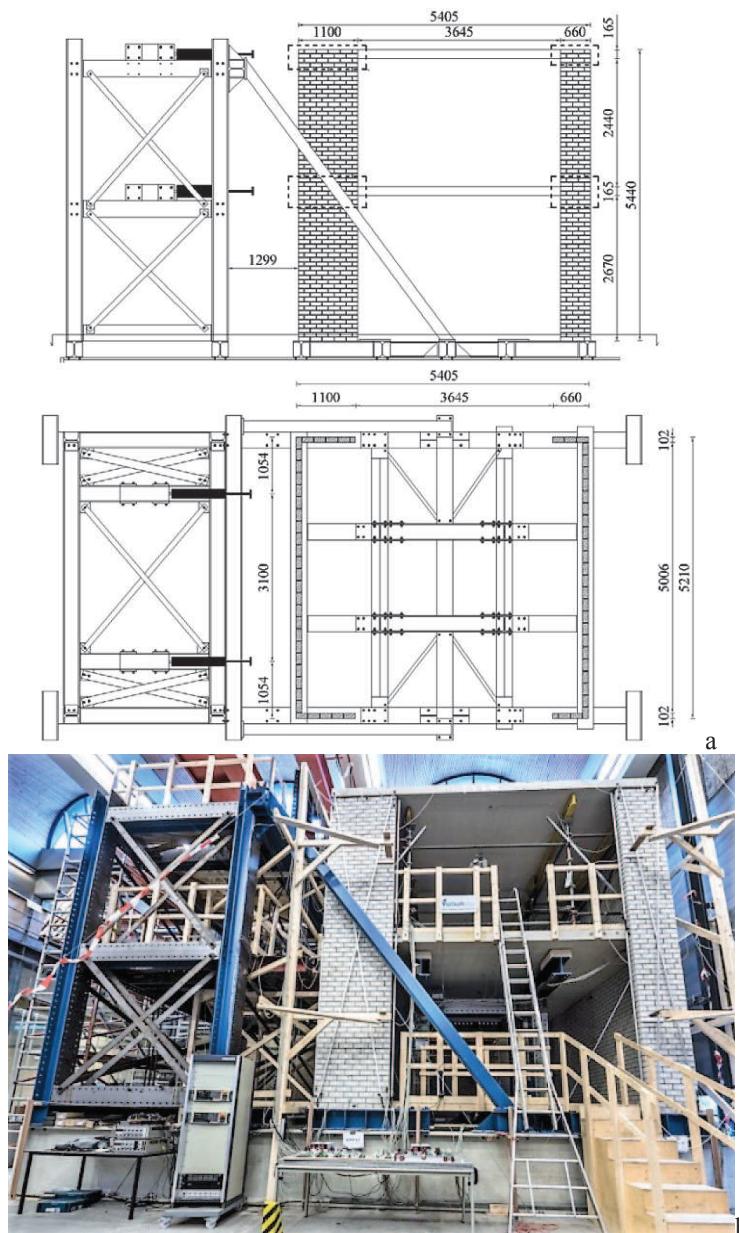

Fig. 9 – Calcium silicate brick masonry terraced house: sketch of the geometry (a) and photo (b).

4   Calibration of the mechanical properties from small-scale tests

The mechanical characterization of the proposed damaging block-based model has been performed following the scheme depicted in Fig. 7, thanks to the small-scale monotonic tests performed on calcium silicate brick masonry at the TU Delft [53] (briefly described in section 3).

An example of calibration of the contact mechanical properties for the shear behaviour is shown in Fig. 10. The experimentally-determined values of cohesion (c), initial friction ($\tan\phi$), and residual friction (μ) have been directly implemented in the numerical model, whereas the ultimate slip of the cohesive behaviour (δ_k) and the brittleness parameter ξ have been calibrated to better fit the curves in Fig. 10b. In particular, the value of K_{ss} has been chosen to represent the average of the initial experimental branches.

By inspecting Fig. 10b, the experimental shear stress-displacement curves appear dependent on the applied pre-compression level. Furthermore, the experimental curves show a less significant cohesive behaviour with a prevalence of friction for high levels of pre-compression (see for instance the three experimental curves in the top of Fig. 10b). A unique set of mechanical parameters was chosen for the description of the shear contact behaviour, aiming at representing the averaged experimental response for both the cohesive and frictional parts. Given the uneven experimental response, this leads evidently to some approximations. However, the level of approximation obtained in the shear contact behaviour could be considered suitable for the model purposes.

Fig. 11 shows the mechanical characterization of the compressive nonlinear behaviour of the blocks by means of compression tests on masonry wallets. The numerical model is not able to directly simulate the formation of vertical cracks through-thickness of the blocks (Fig. 11a). However, the continuum damage formulation of the blocks allows to phenomenologically represent the peak and post-peak compressive behaviour of masonry (Fig. 11b) by showing a widespread distribution of compressive damage into the numerical model (Fig. 11c).

The mechanical parameters calibrated from small-scale tests specimens and, then, used in the numerical simulation of panel-scale and full-scale structures are collected in Table 2. Fig. 12 shows the stress-strain uniaxial tensile and compressive relationships adopted for the block in the simulations, obtained through a calibration process, as shown in Fig. 11b. These curves, which adopted for simplicity a linear softening branch, represent the main input for the definition of the plastic-damage constitutive law assumed for the block, which characterize both the strength and the brittleness of the material. In particular, the tensile curve (Fig. 12a) corresponds to a value 0.41 N/mm of tensile fracture energy, whereas the compressive curve (Fig. 12b) corresponds to a value 11.22 N/mm of compressive fracture energy, being the characteristic length related to the hexahedral finite elements (55 mm x 55 mm x 80 mm) used throughout this study, defined as specified in the Appendix, equal to 55 mm.

The tensile and compressive scalar damage variables, which in theory can assume any value from 0 to 1, have been limited to 0.9 to increase the numerical convergence of the simulations (Table 2), as commonly carried out when using plastic-damage constitutive laws [55]. For this reason, as well as the limitation of the softening regime to a residual value of stress (for the same purpose), the post-peak branch in Fig. 11b is characterized by a (small) residual strength.
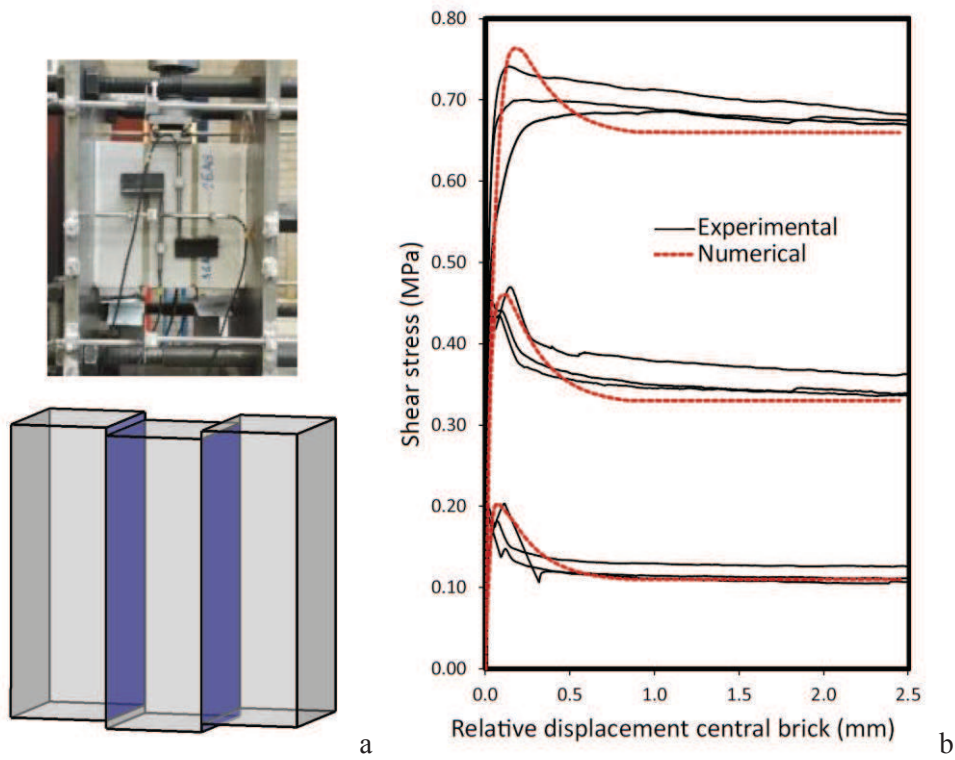
Fig. 10 – Shear tests on triplets: experimental (top) and numerical (bottom) samples (a) and experimental-numerical shear stress – relative displacement of the central brick curves (b) for three different level of pre-compression.
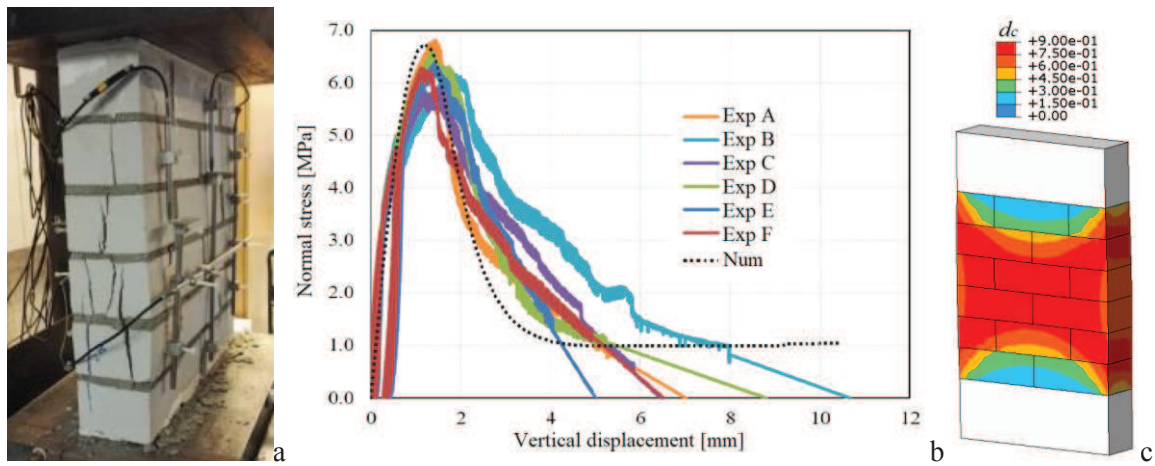

Fig. 11 – Compression tests on masonry wallets: experimental failure (a), experimental-numerical normal stress – vertical displacement curves (b), and compressive damage contour plot (c).

Table 2. Mechanical parameters utilized in the numerical simulations.

Contact mechanical properties				
Tensile behaviour			Shear behaviour	
f_t [MPa]	0.12		$\tan\phi$ [\\]	0.52
u_k [mm]	1.0		c [MPa]	0.11
ζ [\\]	8		δ_k [mm]	1.0
K_{nn} [N/m^3]	75·10^9		ξ [\\]	4
			μ [\\]	0.55
			K_{ss} [N/m^3]	7.5·10^9

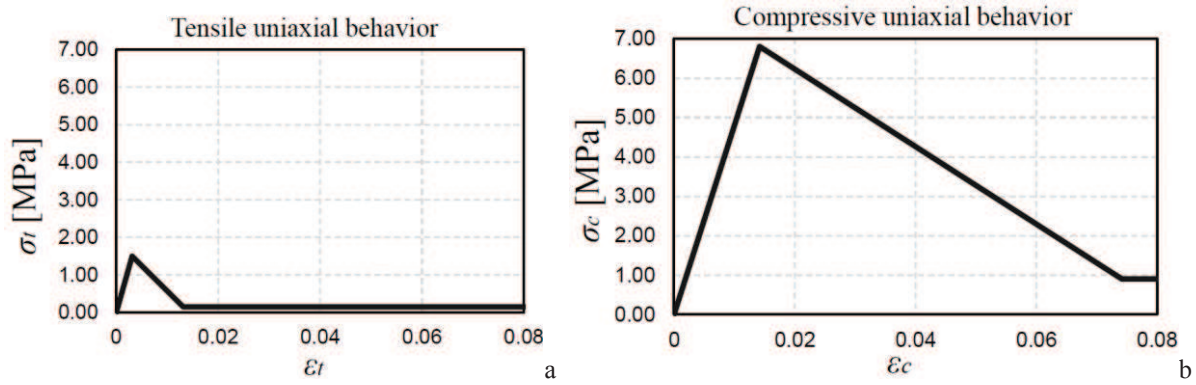| Block mechanical properties					
Young's modulus [MPa]		4800			
Poisson's ratio [\\]		0.17			
Tensile uniaxial nonlinear behaviour			Compressive uniaxial nonlinear behaviour		
Stress [MPa]	Inelastic strain	d_t [\\]	Stress [MPa]	Inelastic strain	d_c [\\]
1.5	0	0	6.8	0	0
0.1	0.01	0.9	0.9	0.06	0.9

Fig. 12 – Stress-strain uniaxial relationships adopted for the block: a) tensile and b) compressive uniaxial curves.

5 Numerical results and discussion

In this section, the results of the performed numerical simulations are critically compared with the experimental outcomes. In particular, two tests of in-plane cyclic loaded walls (with two height/width aspect ratios, i.e. 0.7 and 2.5), one two-way bending cyclic out-of-plane test of a wall, and one cyclic pushover test on a terraced masonry house have been simulated. For the sake of consistency, all the simulations have been conducted by using the mechanical properties collected in Table 2, and the discretization of the block shown in Fig. 1.

A quasi-static direct-integration implicit dynamic analysis algorithm [37] has been adopted in the simulations. This algorithm allows to analyse quasi-static responses in which inertia effects are essentially introduced to regularize unstable behaviours. The Authors experienced a better performance of this algorithm, specifically in the softening and cyclic regime, with respect to more common arc length procedures [35]. Geometric nonlinearity has been considered in the analyses to account for large-displacement effects.

5.1 In-plane cyclic behaviour of walls

The cyclic in-plane tests COMP-2 (slender wall, height/width aspect 2.5) and COMP-6 (thick wall, height/width aspect 0.7) [51] have been considered and simulated. Both walls are characterized by a cantilever configuration. The walls have been modelled through the damaging block-based model herein presented, by

considering a continuum quasi-rigid element on the top to prevent the warping of the wall, following the constraints of the experimental set-up.

The pseudo-time-history of the top displacement experimentally recorded has been applied to a top node of the model (in the centre of the quasi-rigid element), and the pseudo-time-history of the resultant of the base shear has been measured.

Concerning the slender wall COMP-2 test, the comparison between experimental and numerical shear force against measured net displacement curves is shown in Fig. 13, where the numerical monotonic response of the wall is collected as well. The experimental and numerical crack patterns are shown in Fig. 14, where the numerical one is taken at the instant represented by the green circle in Fig. 13. A good agreement between the results is particularly observed for the prediction of the maximum shear load. In this regard, the cyclic and monotonic simulations presented practically the same maximum shear force. The experimental test showed a crack pattern characterized by the combination of rocking and sliding (Fig. 14a) that gives a non-negligible energy dissipation (Fig. 13). Although the dissipation during the cycles, which plays a crucial role in the seismic response of structures, was not fully captured by the model, where almost-pure-rocking was recorded in the first cycles (Fig. 13), dissipation occurred in the model for wider cycles due to masonry crushing (Fig. 14c), see Fig. 13.
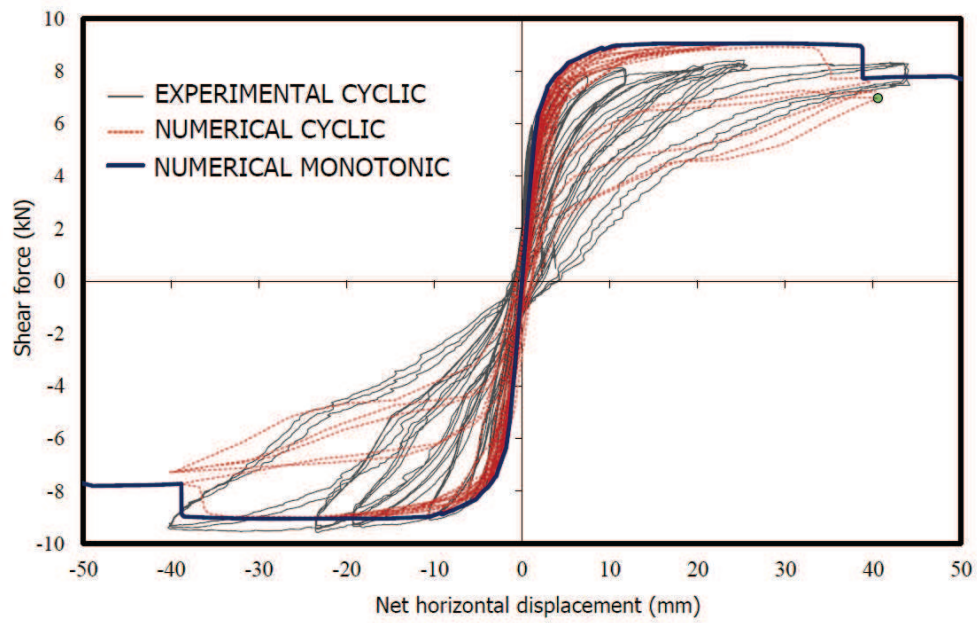
Fig. 13 – Shear force vs measured net displacement of the slender wall COMP-2: comparison between experimental and numerical (cyclic and monotonic) results.
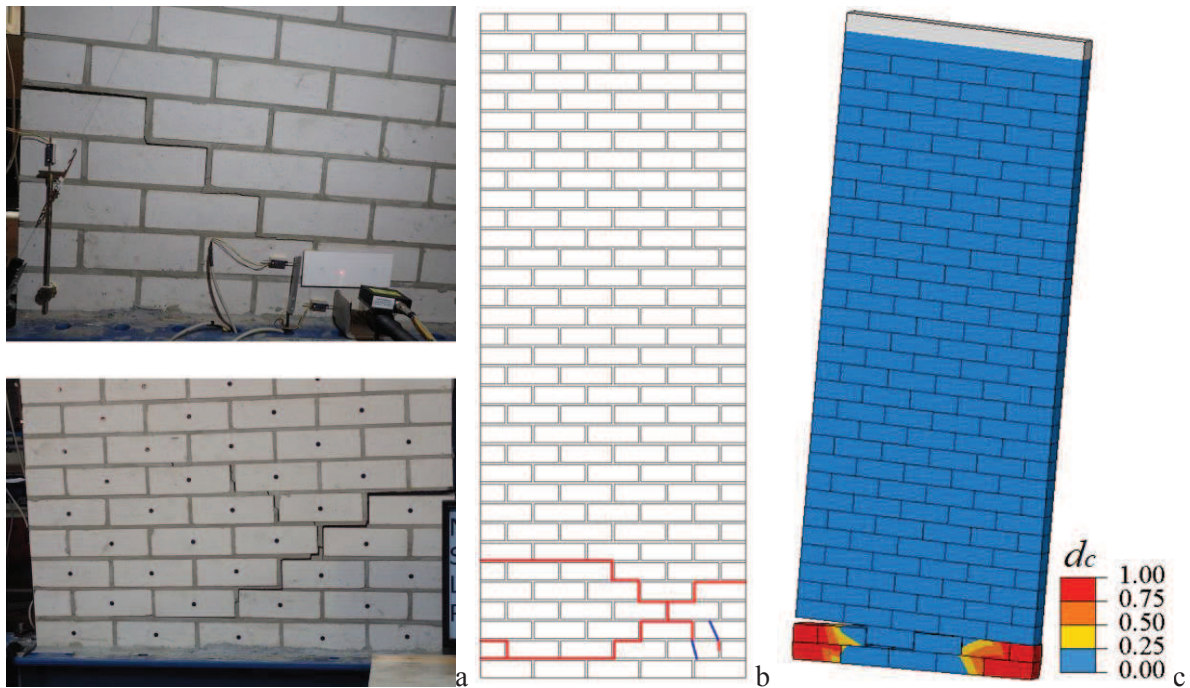

Fig. 14 – Slender wall (COMP-2) crack pattern: photos of the cracked wall (a), experimental crack pattern (b) and numerical compressive damage contour plot (c).

20

Conversely, the thick wall COMP-6 (whose shear force against displacement curves are depicted in Fig. 15, experimental and numerical crack patters in Fig. 16, and compressive and tensile damage contour plots Fig. 17) was mainly characterized by shear failure (Fig. 16a). The hysteretic behaviour of the wall has been rather well predicted by the model, in terms of maximum shear force (Fig. 15), energy dissipation (Fig. 15) and crack pattern (Fig. 16a-b). The deformed horizontal displacement contour plot of Fig. 16b has been taken at the instant represented by the green circle in Fig. 15. It is worth to note that, although taken at an almost-null top horizontal displacement (Fig. 15), significant residual horizontal displacements are recorded at the two sides of the wall, which determine the formation of wide x-shaped shear cracks (Fig. 16b). Likewise, residual horizontal displacements have also been recorded during the experimental test. The numerical cyclic analysis diverged before the full-simulation of the experimental loading path (the non-simulated path has been reported in Fig. 15 through a grey colour), since two half-bricks at the base of the wall slid off as shown in Fig. 16b. It should be noted, anyhow, that the simulation of the considered test is extremely challenging given the co-existence of different failure mechanisms, and damage both along mortar joints (opening and sliding, Fig. 16b) and in the bricks (crushing and splitting, Fig. 17). Also in this case, the in-plane cyclic and monotonic simulations presented a very similar maximum shear force.

To evaluate the sensitivity of the model to the main mechanical properties, several monotonic analyses have been performed on the COMP-6 configuration and the results have been compared (Fig. 18). In particular, the results of the "Reference" analysis, conducted with the mechanical properties collected in Table 2, have been compared with the analyses "PAR_A" (characterised by doubled values of f_t and u_k), "PAR_B" (doubled values of c and δ_k), "PAR_C" (doubled values of $\tan\phi$ and μ), "PAR_D" (doubled values of f_c and G_f), and "PAR_E" (doubled values of all the aforementioned parameters), in terms of shear force against horizontal displacement curves and crack patterns (Fig. 18). The overall behaviour of PAR_A and PAR_D appears akin to the Reference one, whereas PAR_B and PAR_C show a considerable greater maximum shear capacity. In particular, all the analyses showed a shear failure in the wall, exception made for PAR_B which initially showed a bending failure and, subsequently, a sudden shear failure just before a horizontal top displacement of 10 mm. This phenomenon is highlighted in the shear-displacement curve of Fig. 18 by a significant drop of the PAR_B curve. Conversely, the response of PAR_E is completely different, characterized by a bending failure and with a considerably greater shear capacity. Therefore, a significant influence on the shear response of the wall of the contact shear cohesion c and δ_k, as well as contact frictional contributions $\tan\phi$ and μ is observed, as expected. A completely different parameters setting, e.g. PAR_E, gives also a completely different response of the wall, confirming the relevance of the use of correct material parameters.
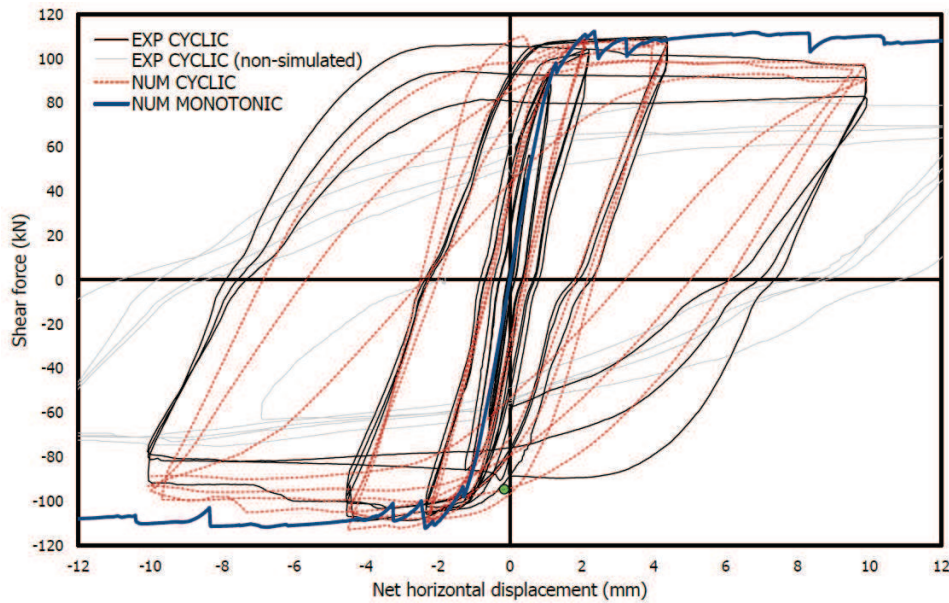

Fig. 15 – Shear force vs measured net displacement of the thick wall COMP-6: comparison between experimental and numerical (cyclic and monotonic) results.
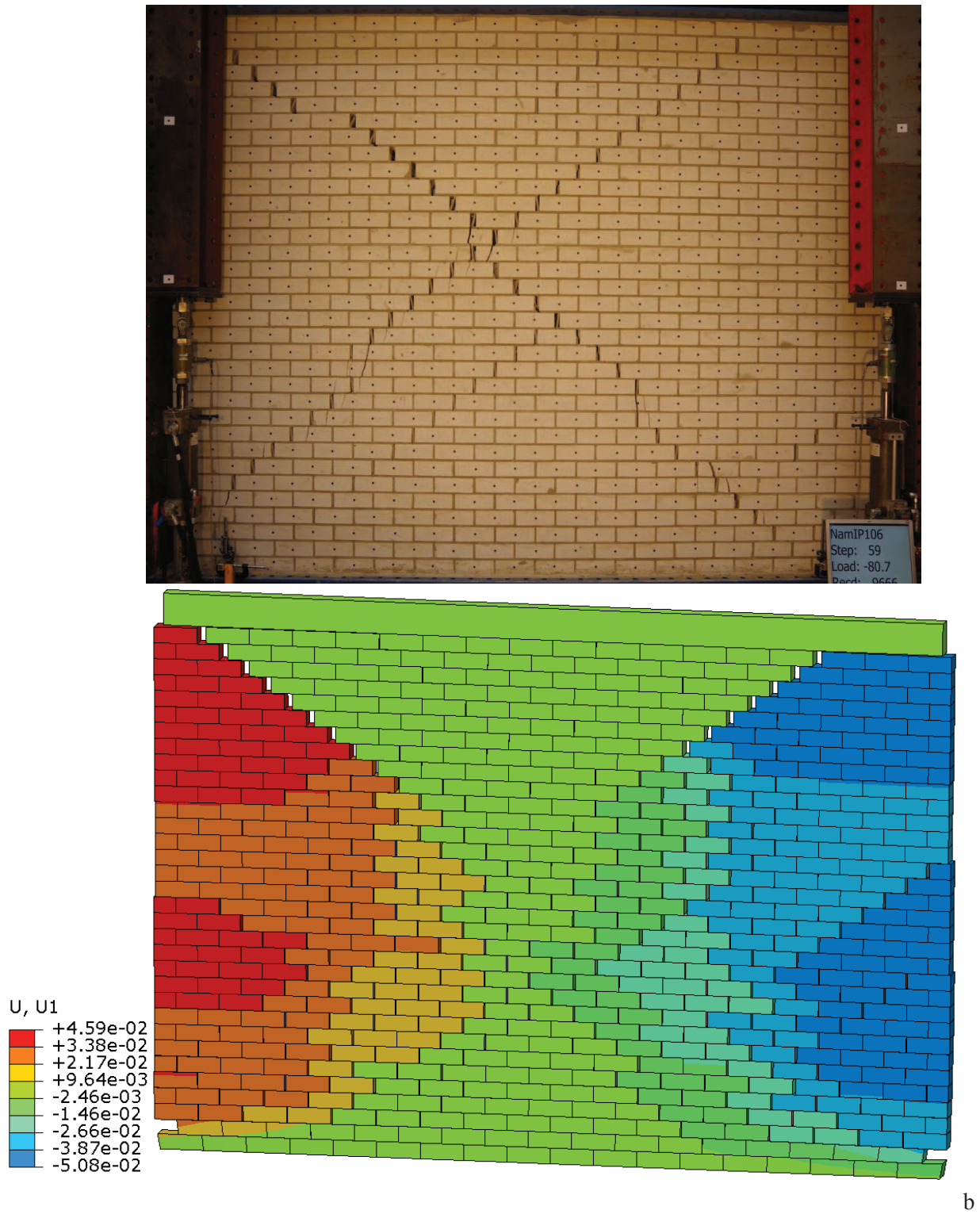
Fig. 16 – Thick wall (COMP-6) crack pattern comparison: photo of the cracked wall (a) and deformed horizontal displacement contour plot (b) in meters.
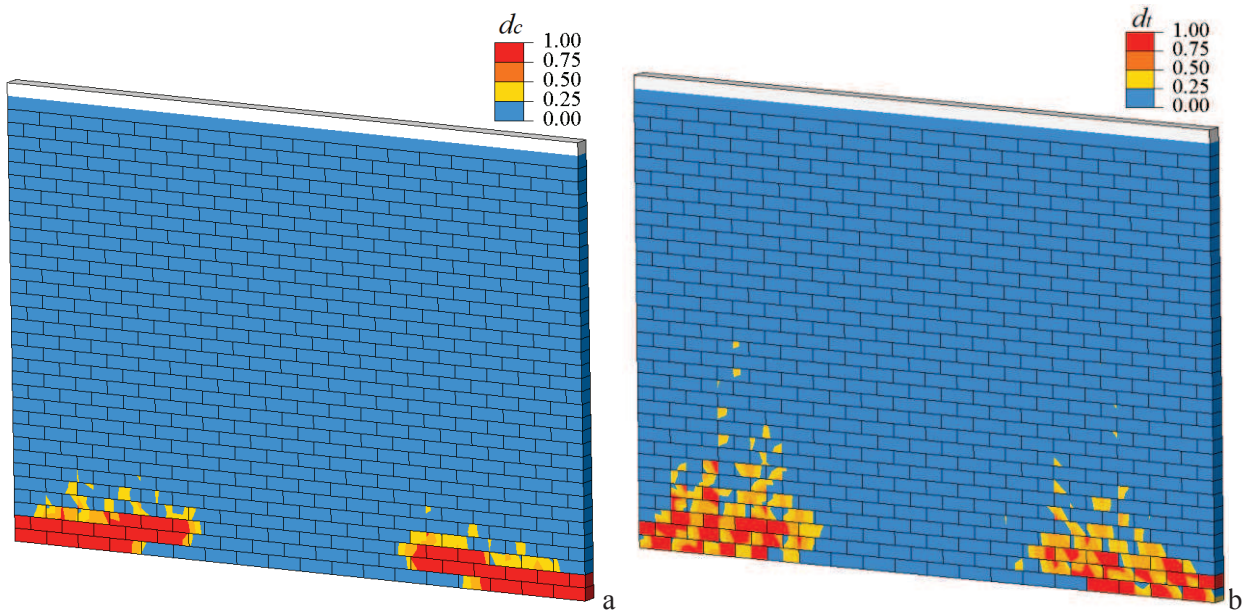
Fig. 17 – Compressive (a) and tensile (b) damage contour plots for the thick wall (COMP-6) at the end of the simulation.
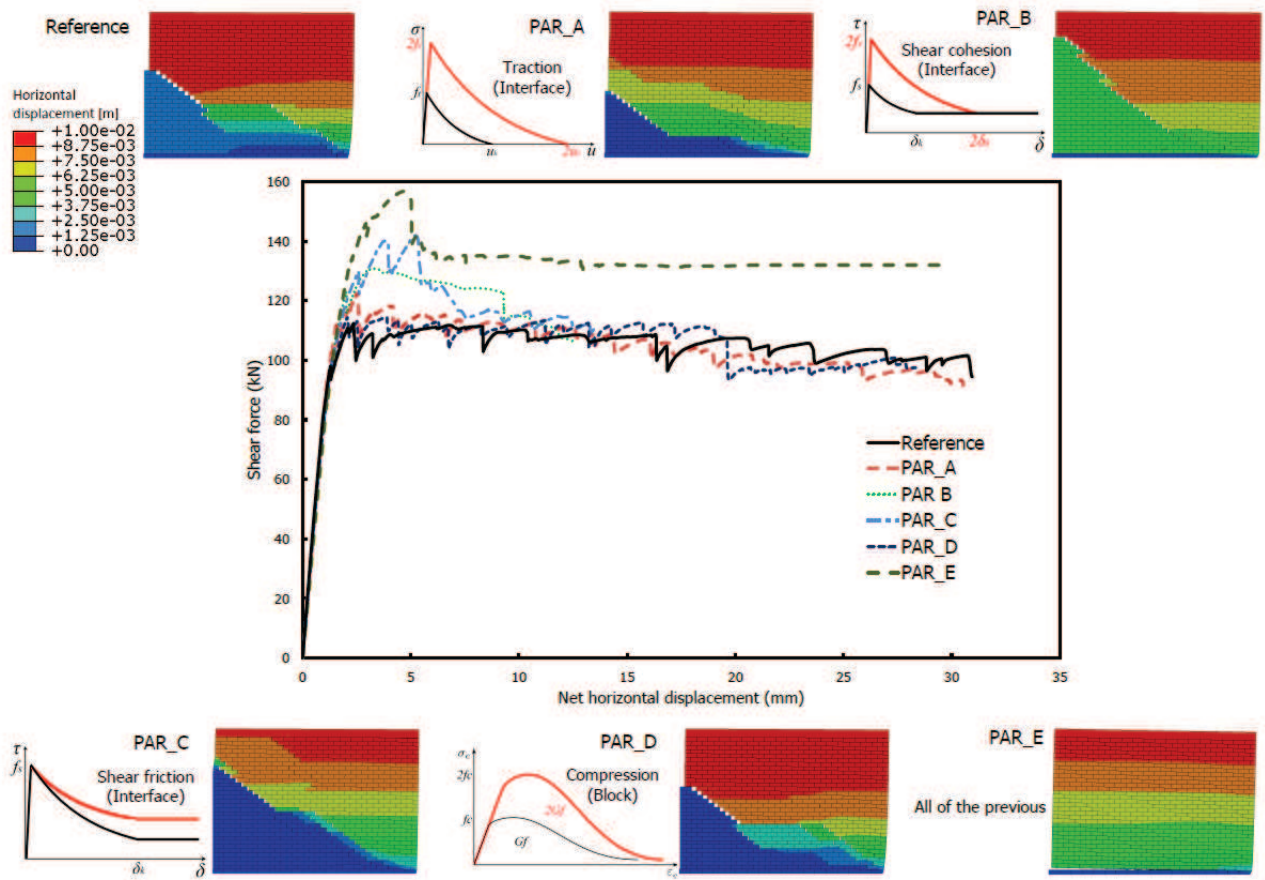

Fig. 18 – Sensibility analysis on the main mechanical parameters of the model. The horizontal displacement contour plots have been taken at a horizontal displacement of 10 mm.

5.2   Out-of-plane cyclic behaviour of walls

The two-way spanning out-of-plane cyclic test COMP-11 conducted on a 3.874x2.765x0.102 m calcium silicate brick masonry wall has been considered and simulated. It has to be pointed out that the experimental set-up conceived for this test needed a considerable level of complexity in order to perform a cyclic out-of-plane test. Indeed, after the application of a vertical pressure (0.05 MPa) to the wall, a constant pressure was applied by the airbag on one side of the wall and a varying pressure by the airbag on the other side of the wall. The pressure in the airbag on the active side was adjusted to achieve the target deformation of a selected set-point; the pressure on the opposite side (passive side) remained constant during each test. Therefore, the set-up allowed for a displacement-controlled test.

To be able to reproduce numerically this complex loading protocol, a non-standard analysis procedure has been conceived and followed. Firstly, a uniform horizontal pressure is monotonically applied to one side of the wall and the equilibrium is investigated through the aforementioned quasi-static implicit dynamic algorithm. The solution is computed until a target displacement (the same considered in the experimental test). Then, a restart of the analysis is carried out: the previous analysis step is ended and a new step which consider a uniform horizontal pressure with an inverted sign is computed. In this way, the cyclic out-of-plane response of the wall is analysed.

The comparison between experimental and numerical lateral force against out-of-plane displacement curves for COMP-11 specimen is shown in Fig. 19, where the numerical monotonic out-of-plane response is collected as well. The experimental and numerical crack patterns are shown in Fig. 20, where the numerical one is taken at the instant represented by the green circle in Fig. 19. A good agreement between the numerical and experimental outcomes is observed. The peak loads are well predicted by the numerical cyclic analysis for the first cycles. Then, the numerical model showed a greater degradation than the experimental test. The analysis has been stopped in correspondence of the green circle in Fig. 19, as, notwithstanding the change in direction of the horizontal pressure, the wall was continuing to deform in the same direction, suggesting the collapse of the wall. It has to be pointed out that, although the model carefully simulates the experimental set-up, the presence of the airbags in the two sides of the wall definitely increases the stability of the wall. In addition, unlike the in-plane benchmarks, a considerable difference between the cyclic and monotonic numerical responses is observed in terms of peak loads. Nevertheless, a sensible difference in peak loads is also observed in the experimental test between positive and negative responses [51], suggesting that the cyclic loading can influence the magnitude of the peak loads.

An excellent agreement is observed from the comparison of the crack patterns in Fig. 20. The model appears able to well-represent the failure mode of the two-way spanning wall (Fig. 20), characterized by diagonal cracking from the wall edges to the centre of the panel, and horizontal cracks at the wall base, at an intermediate height, and at the top of the wall [51]. Indeed, most of the cracks are predicted with a very high accuracy.
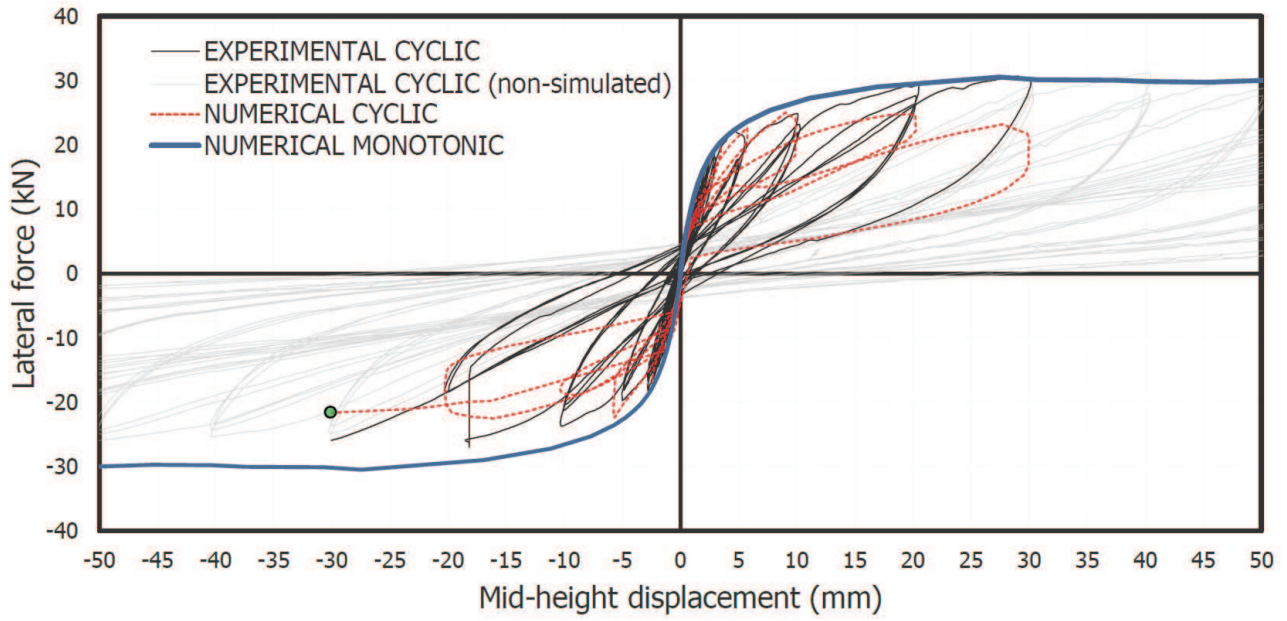
Fig. 19 – Experimental and numerical lateral force against out-of-plane displacement curves for COMP-11 specimen.
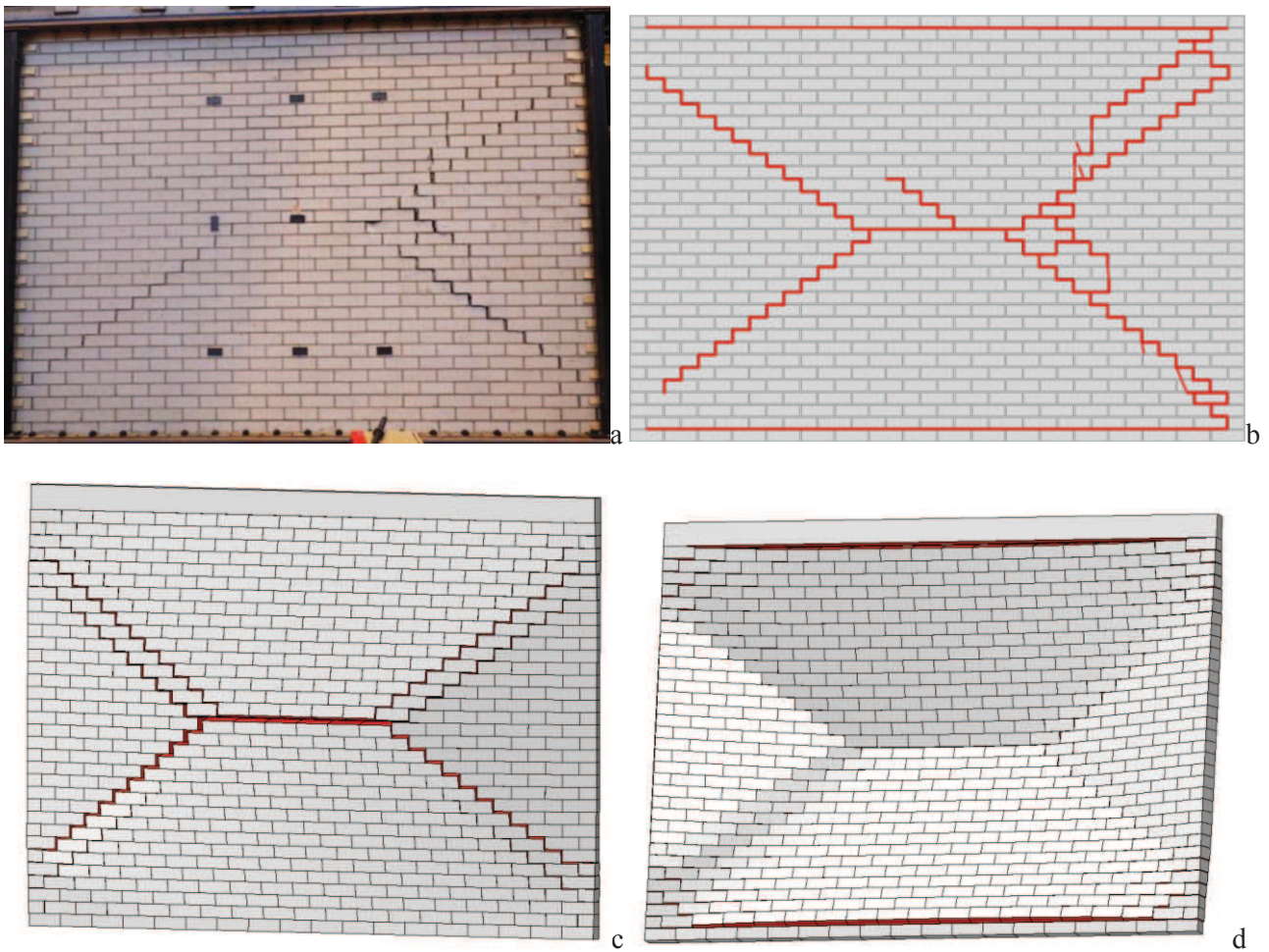

Fig. 20 – Out-of-plane benchmark crack pattern comparison. Specimen COMP-11 crack pattern after removing the airbags: photo (a) and sketch (b). Numerical crack pattern: front (c) and back(d) views.

5.3   Cyclic behaviour of a full-scale masonry structure

The quasi-static cyclic pushover test conducted on the terraced masonry house shown in Fig. 9 has been modelled and simulated. Numerical cyclic and monotonic analyses have been performed on a half-house model, given the symmetry of the structure and of the loading conditions. The numerical results in terms of base shear against horizontal displacement of the top floor have been collected and compared with the experimental ones in Fig. 21. The "numerical cyclic actual" analysis (Fig. 21) has been conducted by imposing the actual time-history of the horizontal displacement measured at the two floor levels. Differently, the "numerical cyclic reduced" analysis consisted of a reduced number of cycles. Particularly, a set of equal forces has been monotonically applied to the two floors of the structure until the top floor reached a target displacement and, then, the analysis has been stopped. Successively, a restart analysis has been performed by inverting the sign of the forces. This procedure has been repeated a certain number of times by increasing the magnitude of the top target displacement. Finally, also monotonic analyses have been performed in two directions. The crack pattern of the "numerical cyclic reduced" analysis are collected and compared with the experimental cracks in Fig. 22, while the tensile and compressive damage contour plots at the end of the simulation are shown in Fig. 23. The deformed shape and the tensile and compressive damage contour plots for the positive and negative "numerical monotonic" analyses are collected in Fig. 24 and Fig. 25, respectively.

An overall positive correspondence between experimental and numerical curves can be observed in Fig. 21. The "numerical cyclic actual" analysis is untimely stopped due to divergence in the solution of the continuum nonlinear equations in a single block. Differently, although ended for the same reason, the "numerical cyclic reduced" analysis was able to proceed further, until significant top displacements (e.g. ±60 mm). Anyhow, the prediction of the peak shear force for both cases is in good agreement with the experimental one (Fig. 21). Interestingly, for the "numerical cyclic reduced" analysis a degradation of the shear force is observed in the positive direction for subsequent cycles, while no particular degradation is observed in the negative direction. This aspect appears particularly valuable as it is also an experimental trend (Fig. 21), determined by the different width of the two piers of the house [52]. Furthermore, concerning the monotonic response of the model, in the positive direction the shear base is characterized by a peak load, followed by a significant softening until about +20 mm and, then, by a plateau, while in the negative direction, once reached the peak load, it remains practically constant. The differences in the peak load between the numerical cyclic and monotonic responses are irrelevant for the negative direction, while they are significant in the positive direction, suggesting that the failure mechanism which occurs in the positive direction is influenced and degraded by a cyclic action, whereas the one which occurs in the negative direction appears independent from that. Generally, the numerical model tends to underestimate the dissipation during the cycles (Fig. 21).

The actual crack pattern experienced by the structure appears very complex and characterized by a combination of in-plane and out-of-plane failure mechanisms [52]. The comparison of the "numerical cyclic reduced" deformed shapes with the actual crack pattern shows the very good accuracy of the model which accounts for the main failures of the structure (Fig. 22). Particularly, the shear-vertical crack experienced by the structure in the wider (left) pier (see Fig. 22, top) is well-predicted by the model which shows a series of contact shear failures as well as a vertical distribution of tensile damage in the blocks (Fig. 22, top), standing for a vertical crack which crosses the blocks as well (which is an experimental outcome too). Besides, the interaction of the piers with the transversal walls, due to the running bond texture, is fairly captured by the model. The different failure mechanism that develops in the piers for the two loading directions can be clearly observed also by comparing the deformed shapes of the model in the positive (+50 mm) and negative (–50 mm) directions (Fig. 22 and Fig. 23 for the cyclic analyses, and Fig. 24 and Fig. 25 for the monotonic analyses): while the wider (left) pier shows a shear-vertical failure in the lower level when loaded in a positive direction, it shows a completely different mechanism, i.e. almost-pure rocking, when loaded in a negative direction. This also explains the different post-peak direction observed for the two loading directions. Again, the role of the transversal walls and their connection to the piers appears crucial in the structural response.

Finally, the cyclic evolution of the resultant of the vertical reaction for the walls of the structure depending on the horizontal displacement of the second floor is shown in Fig. 26 for the "numerical cyclic reduced" analysis. This outcome allows to further investigate the cyclic response of the structure. Indeed, the cyclic redistribution of the vertical load between the transversal wall W1 (W2) and the pier P1 (P2), see Fig. 26, appears particularly interesting, as, for instance, the first floor is connected in no way with the piers and it only stands on the

26

transversal walls. Therefore, the load transfer passes through the corner, thanks to the toothing of the walls. In the negative direction, the vertical load is mainly borne by W1 and P2 (Fig. 26). In particular, by increasing the top displacement in the negative direction, the vertical load is gradually transferred from W2 to P2 and at about –20 mm the vertical load is completely transferred and the wall W2 is completely unloaded. Conversely, in the positive direction the vertical load is mainly borne by W2 and P1 (Fig. 26). If the load transfer between P2 and W2 follows a regular evolution, suggesting the activation of a pure rocking mechanism, the load transfer between P1 and W1 appears more complex in the positive direction, where the unloading path is different from the loading one (Fig. 26). Once more, this aspect suggests a more complex failure mechanism in the positive direction.
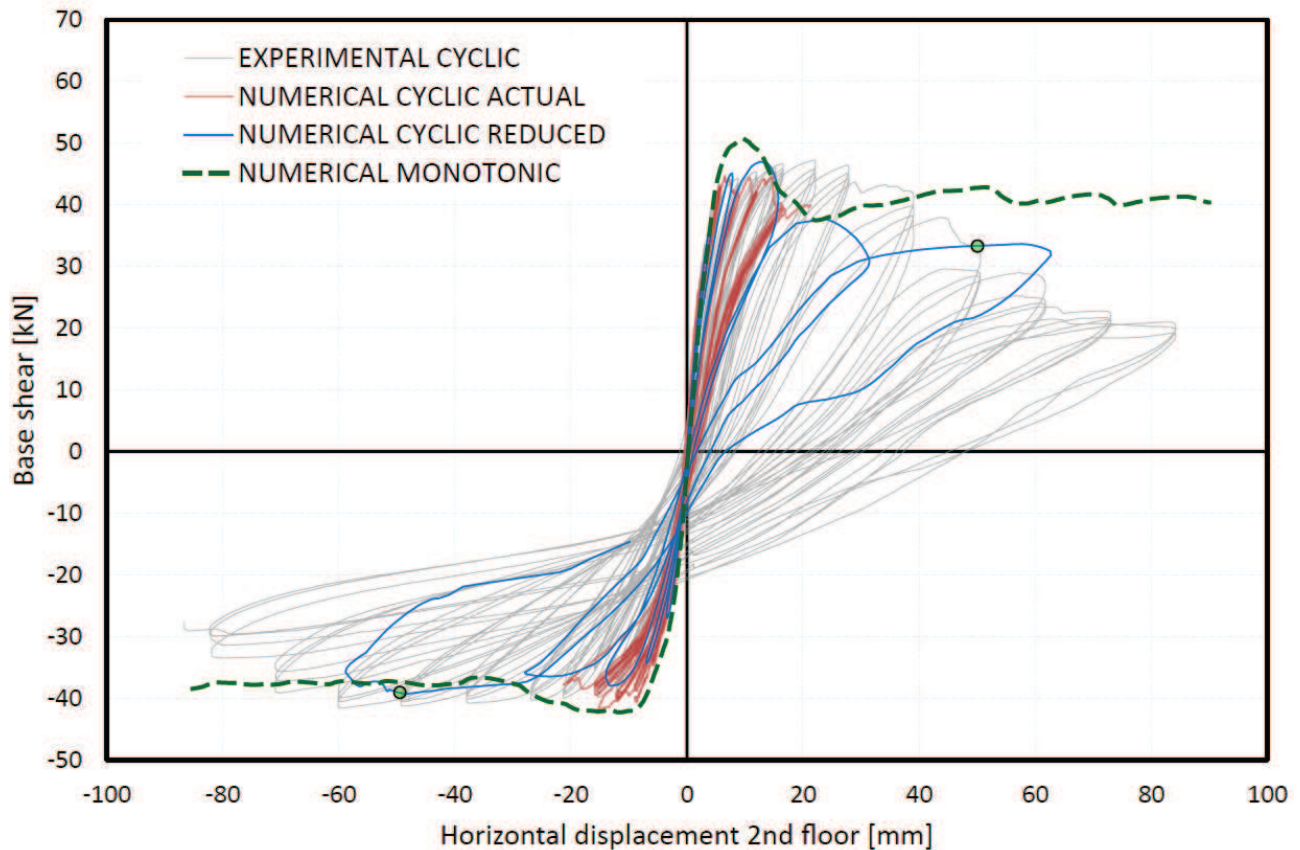

Fig. 21 – Terraced house base shear – horizontal displacement experimental-numerical comparison.
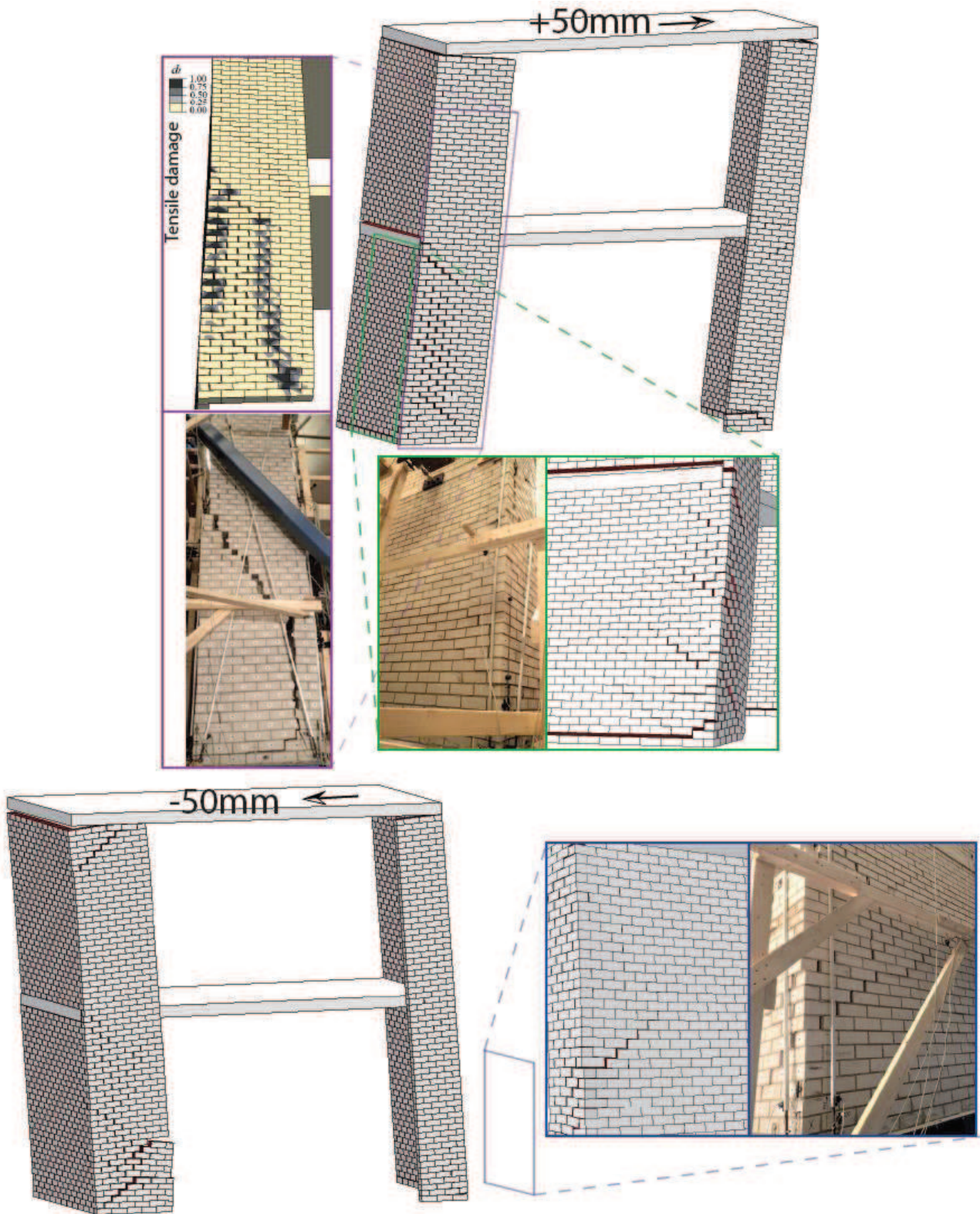
Fig. 22 – Numerical cyclic reduced analysis: deformed shapes and comparisons with the actual crack pattern. The numerical plots are taken in correspondence of the two green circles in Fig. 21, for a top displacement ±50 mm, whereas the photos are taken during the last cycle of the experimental test.
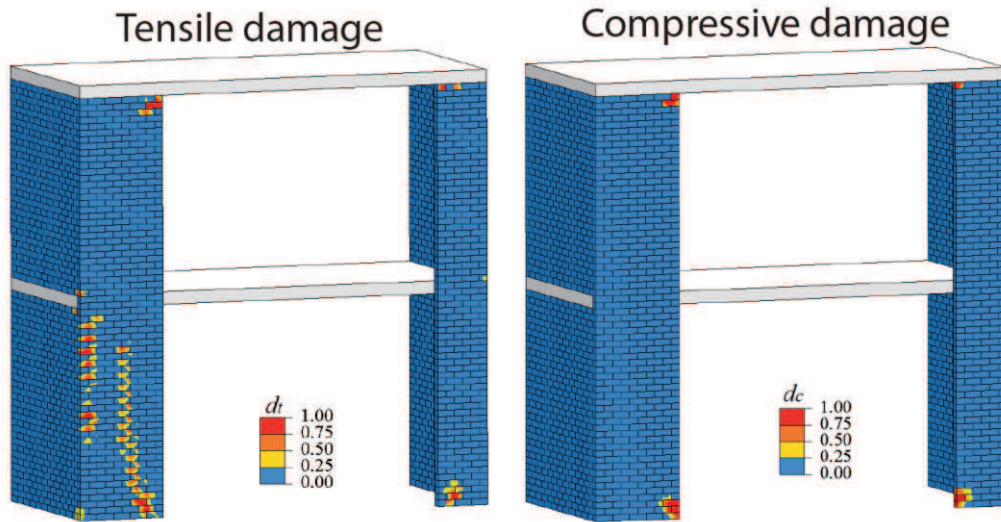
Fig. 23 – Numerical cyclic reduced analysis: tensile and compressive damage contour plots at the end of the simulation.
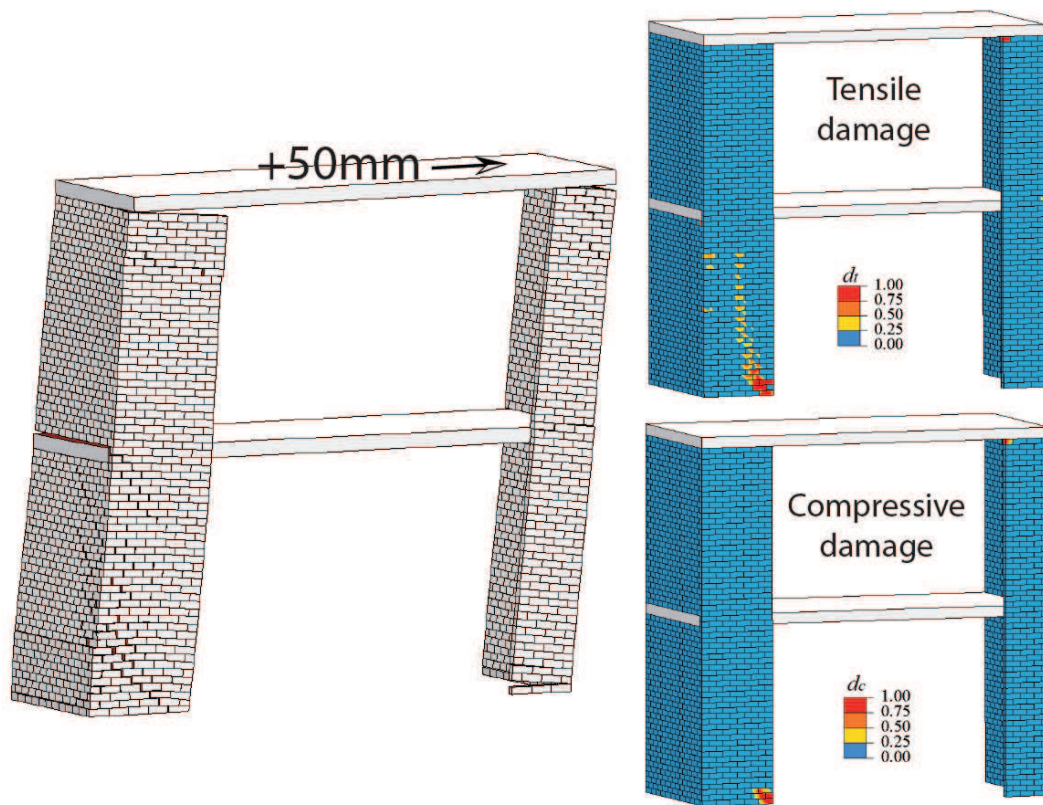

Fig. 24 – Numerical monotonic simulation in the positive direction: deformed shape at +50mm (left) and tensile and compressive damage variables contour plots.
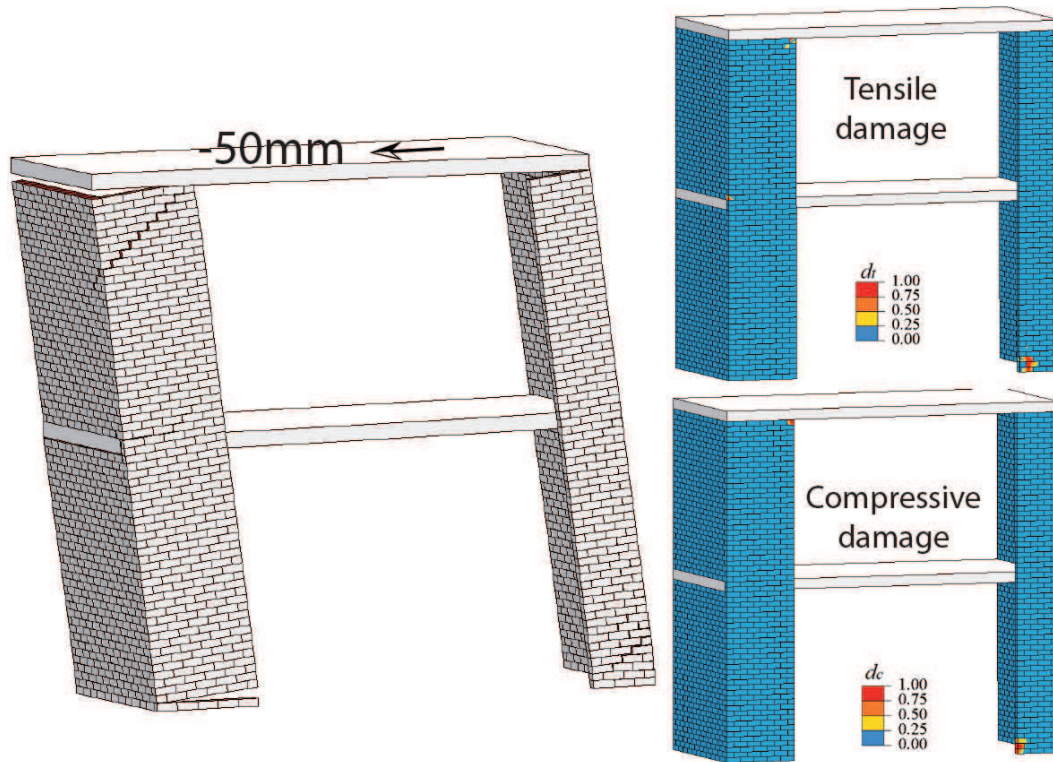
Fig. 25 – Numerical monotonic simulation in the negative direction: deformed shape at -50mm (left) and tensile and compressive damage variables contour plots.
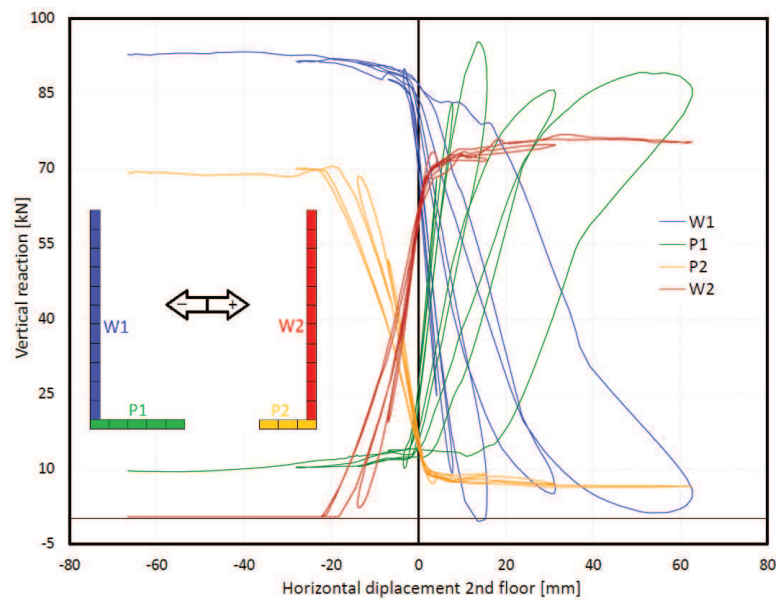

Fig. 26 – Numerical cyclic reduced analysis: resultant of the vertical reaction for the walls depending on the horizontal displacement of the second floor.

6   Conclusions

In this paper, a novel damaging block-based model for the numerical analysis of the cyclic behaviour of full-scale masonry structures has been proposed. Solid 3D finite elements governed by a plastic-damage constitutive law in tension and compression have been used to model the blocks, while a cohesive-frictional contact-based formulation has been developed to simulate their cyclic interaction.

The mechanical characterization of this novel modelling approach can be easily carried out, as it requires only simple monotonic tests on small-scale masonry specimens. A strategy for the comprehensive mechanical characterization of the mechanical properties of the numerical model from these small-scale experiments has been proposed.

A comprehensive experimental campaign on calcium silicate brick masonry specimens has been used to validate the proposed calibration procedure, and to assess the accuracy of the modelling approach at structural level. Once defined the mechanical parameters from small-scale tests, they have been used in the simulation of in-plane and out-of-plane cyclic tests on masonry walls made of the same material. An overall good agreement between the numerical results and the experimental outcomes has been observed both in the in-plane and out-of-plane responses. This allowed to validate the model as well as the strategy proposed for its mechanical characterization.

Furthermore, a cyclic pushover test on a full-scale terraced masonry house has been simulated using the same mechanical parameters calibrated from small-scale tests. Good results have been obtained, showing the reliability of the model, although the numerical model tends to underestimate the dissipation during the cycles. Further thorough comparisons between numerical and experimental data also in terms of dissipation during the cycles will be carefully carried out in the future. However, given the accuracy of the model and its capability to explicitly account for structural details such as running bonds, toothing between walls, the actual masonry texture, etc. which can be crucial in the structural response, the model can also be used to interpret the results of full-scale complex experimental tests.

Finally, the efficiency of the model is also shown by its limited computational effort. Indeed, although a full-scale terraced masonry house has been considered, all the analyses have been performed on a commercial laptop in a reasonable amount of time. By way of example, the average time needed for the monotonic pushover analyses on the full-scale terraced house, carried out on a laptop equipped with a processor Intel®Core™ i7-6500U CPU @ 2.50GHz and 16GB RAM, was 2 hours and 9 minutes.

Therefore, although some further advances in the robustness of the solving algorithm should be developed, the model here proposed represents an efficient and reliable tool to analyse the cyclic behaviour of masonry structures.

APPENDIX

The main features of the plastic-damage model developed by Lee and Fenves [36] are here presented. Isotropic degradation damage is assumed and, if a scalar degradation damage variable $0 \leq d < 1$ is used to represent the isotropic damage and the concepts of strain decomposition and effective stress are employed, then the Cauchy stress tensor $\boldsymbol{\sigma}$ becomes:

$$\boldsymbol{\sigma} = (1-d)\overline{\boldsymbol{\sigma}} = (1-d)\boldsymbol{E_0}(\boldsymbol{\varepsilon} - \boldsymbol{\varepsilon^p}), \qquad (9)$$

where $\overline{\boldsymbol{\sigma}}$ is the effective stress tensor, $\boldsymbol{E_0}$ is the initial undamaged elastic stiffness tensor, $\boldsymbol{\varepsilon}$ is the strain tensor and $\boldsymbol{\varepsilon^p}$ is the plastic part of the strain tensor.

The plastic strain rate is obtained from a plastic potential Φ defined in the effective-stress space:

$$\dot{\boldsymbol{\varepsilon}}^p = \dot{\lambda}\frac{\partial\Phi(\overline{\boldsymbol{\sigma}})}{\partial\overline{\boldsymbol{\sigma}}}, \qquad (10)$$

where $\dot{\lambda}$ is the plastic multiplier ($\dot{\lambda} \geq 0$). To control dilatancy, a nonassociative flow rule is considered. Particularly, the plastic strain rate is obtained by a flow rule generated by a Drucker-Prager type plastic potential, which, in terms of effective stresses, has the form:

$$\Phi = \sqrt{(\epsilon f_{t0}\tan\psi)^2 + 3J_2(\overline{\boldsymbol{\sigma}})} + \frac{1}{3}I_1(\overline{\boldsymbol{\sigma}})\tan\psi, \qquad (11)$$

being I_1 the first invariant of the stress tensor, J_2 the second invariant of the stress deviator, f_{t0} the initial uniaxial tensile strength, ϵ a smoothing constant generally assumed equal to 0.1 [45], and ψ the dilatancy angle of the quasi-brittle material, typically assumed equal to 10° in agreement with experimental evidences [44] and previous numerical models [45, 46].

The stress admissibility condition reads as:

$$F(\overline{\boldsymbol{\sigma}}, \varsigma_t, \varsigma_c) \leq 0, \qquad (12)$$

where ς_t and ς_c are uniaxial tensile and compressive strength functions depending on two hardening variables k_t and k_c:

$$\varsigma_t(k_t) = [1 - d_t(k_t)]\overline{\varsigma_t}(k_t), \quad \varsigma_c(k_c) = [1 - d_c(k_c)]\overline{\varsigma_c}(k_c), \qquad (13)$$

being $\overline{\varsigma_t}(k_t)$ and $\overline{\varsigma_c}(k_c)$ the uniaxial tensile and compressive strengths in the effective-stress responses and the scalar damage variables $d_t(k_t)$ and $d_c(k_c)$ functions of the hardening variables. The degradation damage variable d in (9) is then written as a function of the stress state and the scalar damage variables d_t and d_c as:

$$d = 1 - (1 - s_t d_c)(1 - s_c d_t), \qquad (14)$$

where s_t and s_c are functions of the stress state that are introduced to model stiffness recovery effects associated with stress reversals. Assuming that the material fully recovers the compressive stiffness, they are defined according to the following relationships:

$$s_t = 1 - H(\sigma_{uniaxial}), \qquad s_c = 1 - \left(1 - H(\sigma_{uniaxial})\right), \qquad (15)$$

where

$$H(\sigma_{uniaxial}) = \begin{cases} 1, & \sigma_{uniaxial} \geq 0, \\ 0, & \sigma_{uniaxial} < 0 \end{cases} \tag{16}$$

being $\sigma_{uniaxial}$ the uniaxial stress (positive in tension). Assuming, for instance, an initially undamaged material in compression ($d_c = 0$), the degradation damage variable d becomes

$$d = 1 - \left(1 - \left(1 - (1 - H(\sigma_{uniaxial}))\right)d_t\right), \tag{17}$$

where in tension $H(\sigma_{uniaxial}) = 1$ and, therefore, $d = d_t$ (as expected); whereas in compression $H(\sigma_{uniaxial}) = 0$ and, therefore, $d = 0$, the material fully recovers the compressive stiffness (which in this case is the initial undamaged stiffness, $E = E_0$). Furthermore, d in (14) fulfils the condition $0 \leq d < 1$ and equals d_t when $d_c = 0$ (uniaxial tensile case) and d_c when $d_t = 0$ (uniaxial compressive case). Consequently, the uniaxial strength functions (13) can be written as:

$$\varsigma_t = (1 - d)\bar{\varsigma}_t, \quad \varsigma_c = (1 - d)\bar{\varsigma}_c. \tag{18}$$

Being $\boldsymbol{k} = [k_t, k_c]^T$, the plastic-damage model employs the yielding surface (Fig. 27) proposed in [47] and further developed in [36], which has, in the effective-stress space, the form:

$$F = \frac{1}{1 - \alpha}\left[\alpha I_1(\boldsymbol{\sigma}) + \sqrt{3J_2(\boldsymbol{\sigma})} + \beta(\boldsymbol{k})\langle\bar{\sigma}_{max}\rangle - \gamma\langle-\bar{\sigma}_{max}\rangle\right] + \bar{\varsigma}_c(k_c) = 0, \tag{19}$$

where $\bar{\sigma}_{max}$ is the algebraically maximum principal stress in the effective-stress space, α and γ are dimensionless constants and $\beta(\boldsymbol{k})$ is a function of the hardening variables. The constant α depends on the ratio f_{b0}/f_{c0} between the biaxial initial compressive strength f_{b0} and the uniaxial initial compressive strength f_{c0} through the relationship $\alpha = [(f_{b0}/f_{c0}) - 1]/[2(f_{b0}/f_{c0}) - 1]$. Typically, $f_{b0}/f_{c0} = 1.16$, which implies $\alpha = 0.12$ [47]. The constant γ appears only in triaxial compression and is defined as $\gamma = 3(1 - \rho)/(2\rho - 1)$, where the constant ρ represents the ratio of the second stress invariant on the tensile meridian to that on the compressive meridian at initial yield. Typically, $\rho = 2/3$, which leads to $\gamma = 3$ [47]. Finally, $\beta(\boldsymbol{k})$ is assumed to depend on the hardening variables by the relationship $\beta(\boldsymbol{k}) = -\bar{\varsigma}_c(k_c)/\bar{\varsigma}_t(k_t)(1 - \alpha) - (1 + \alpha)$.
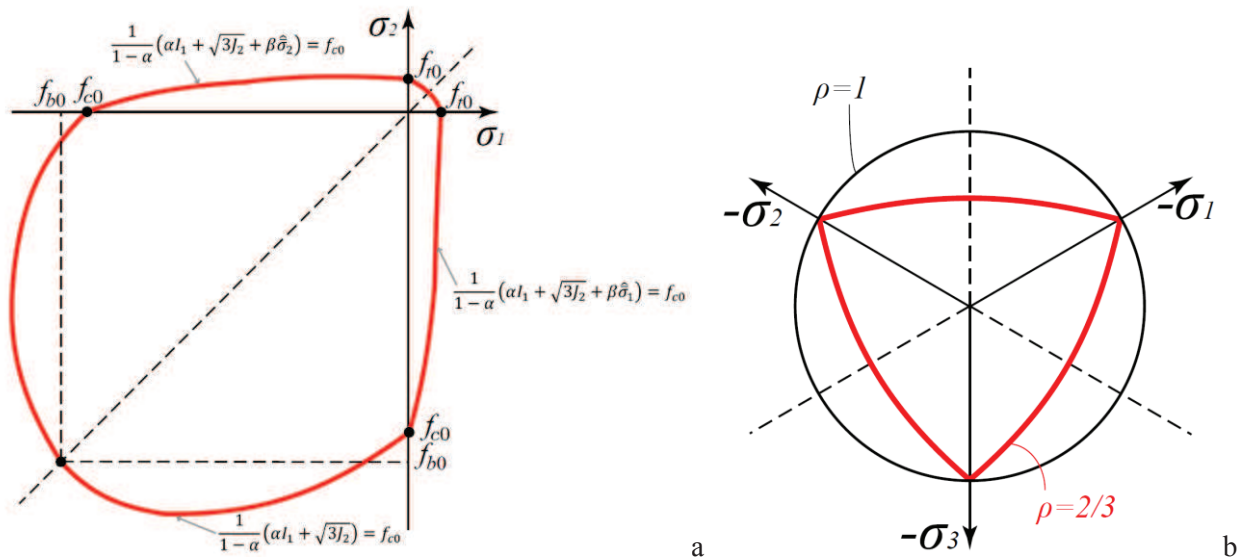

Fig. 27 – Plastic-damage model yielding surface in: a) plain stress and b) the deviatoric plane.

The evolution of the hardening variables is expressed in terms of the eigenvalues of the effective stress and plastic strain rate tensors, collected, respectively, in $\widehat{\overline{\boldsymbol{\sigma}}}$ and $\widehat{\dot{\boldsymbol{\varepsilon}}^p}$, as:

$$\dot{\boldsymbol{k}} = \dot{\lambda}\mathbf{h}(\widehat{\overline{\boldsymbol{\sigma}}}, \boldsymbol{k}, g_t, g_c)\frac{\partial \Phi(\widehat{\overline{\boldsymbol{\sigma}}})}{\partial \widehat{\overline{\boldsymbol{\sigma}}}} = \mathbf{h}(\widehat{\overline{\boldsymbol{\sigma}}}, \boldsymbol{k}, g_t, g_c)\widehat{\dot{\boldsymbol{\varepsilon}}^p},$$ (20)

being

$$\mathbf{h}(\widehat{\overline{\boldsymbol{\sigma}}}, \mathbf{k}, g_t, g_c) = \begin{bmatrix} r(\widehat{\overline{\boldsymbol{\sigma}}})\varsigma_t(k_t)/g_t & 0 & 0 \\ 0 & 0 & (1-r(\widehat{\overline{\boldsymbol{\sigma}}}))\varsigma_c(k_c)/g_c \end{bmatrix},$$ (21)

where the scalar quantity $r(\widehat{\overline{\boldsymbol{\sigma}}})$ is a weight factor ($0 \leq r \leq 1$) defined as $r(\widehat{\overline{\boldsymbol{\sigma}}}) = \frac{\sum_{i=1}^{3}\langle\widehat{\overline{\sigma}}_i\rangle}{\sum_{i=1}^{3}|\widehat{\overline{\sigma}}_i|}$, and the quantities g_t and g_c are the dissipated energy densities in tension and compression, respectively. These are derived from the tensile G_t and compressive G_c fracture energies, which are primary mechanical properties of the material, following the relationships:

$$g_t = G_t/h, \quad g_c = G_c/h,$$ (22)

being h the localization zone size (characteristic length) defined as

$$h = \alpha_h\sqrt{V_e} = \alpha_h\left(\sum_{\rho=1}^{n_\rho}\sum_{\xi=1}^{n_\xi}\sum_{\eta=1}^{n_\eta}\det J w_\rho w_\xi w_\eta\right),$$ (23)

where w_ρ, w_ξ and w_η are the weight factors of the Gaussian integration scheme, J the Jacobian of the transformation, V_e the element area and α_h a modification factor that depends on the typology of the finite element used. In this way, the mesh size does not significantly influence the material response.

Generally, the values of the fracture energies (G_t and G_c), which are primary material parameters that have to be inputted in the model, can be defined either in a direct way, i.e. by directly specifying their values, or in an indirect way, i.e. by the point-by-point specification of the inelastic stress-strain uniaxial curves in tension and compression. Typically, the point-by-point specification of the inelastic stress-strain uniaxial curves in tension and compression is preferred as it allows to specify a residual strength (both in tension and compression) which greatly helps the convergence of the solving algorithm in case of softening.

REFERENCES

[1] S. Invernizzi, G. Lacidogna, N. E. Lozano-Ramírez and A. Carpinteri, "Structural monitoring and assessment of an ancient masonry tower," *Engineering Fracture Mechanics,* 2018 In Press.

[2] M. J. DeJong, M. A. N. Hendriks and J. G. Rots, "Sequentially linear analysis of fracture under non-proportional loading," *Engineering Fracture Mechanics,* vol. 75, no. 18, p. 5042–5056, 2008.

[3] J. G. Rots, F. Messali, R. Esposito, V. Mariani and S. Jafari, "Multi-Scale Approach towards Groningen Masonry and Induced Seismicity," *Key Engineering Materials,* vol. 747, pp. 653-661, 2017.

[4] E. Sacco, D. Addessi and K. Sab, "New trends in mechanics of masonry," *Meccanica,* vol. 53, no. 7, p. 1565–1569, 2018.

[5] S. Lagomarsino, A. Penna, A. Galasco and S. Cattari, "TREMURI program: An equivalent frame model for the nonlinear seismic analysis of masonry buildings," *Engineering Structures,* vol. 56, p. 1787–1799, 2013.

[6] L. Berto, A. Saetta, R. Scotta and R. Vitaliani, "An Orthotropic Damage Model for Masonry Structures," *International Journal for Numerical Methods in Engineering,* vol. 55, no. 2, p. 127–157, 2002.

[7] L. Pelà, M. Cervera, S. Oller and M. Chiumenti, "A localized mapped damage model for orthotropic materials," *Engineering Fracture Mechanics,* Vols. 124-125, p. 196–216, 2014.

[8] D. Addessi and E. Sacco, "Nonlinear analysis of masonry panels using a kinematic enriched plane state formulation," *International Journal of Solids and Structures,* vol. 90, pp. 194-214, 2016.

[9] S. Marfia and E. Sacco, "Multiscale damage contact-friction model for periodic masonry walls," *Computer Methods in Applied Mechanics and Engineering,* Vols. 205-208, p. 189–203, 2012.

[10] B. C. N. Mercatoris, P. Bouillard and T. J. Massart, "Multi-scale detection of failure in planar masonry thin shells using," *Engineering Fracture Mechanics,* vol. 76, no. 4, p. 479–499, 2009.

[11] A. Chettah, B. C. N. Mercatoris, E. Sacco and T. J. Massart, "Localisation analysis in masonry using transformation field analysis," *Engineering Fracture Mechanics,* vol. 110, p. 166–188, 2013.

[12] P. B. Lourenço and J. G. Rots, "Multisurface Interface Model for Analysis of Masonry Structures," *Journal of Engineering Mechanics,* vol. 123, no. 7, p. 660–668, 1997.

[13] S. Casolo, "Modelling in-Plane Micro-Structure of Masonry Walls by Rigid Elements," *International Journal of Solids and Structures,* vol. 41, no. 13, p. 3625–3641, 2004.

[14] L. Macorini and B. A. Izzuddin, "A Non-Linear Interface Element for 3D Mesoscale Analysis of Brick-Masonry Structures," *International Journal for Numerical Methods in Engineering,* vol. 85, no. 12, p. 1584–1608, 2011.

[15] F. Parrinello, B. Failla and G. Borino, "Cohesive–frictional Interface Constitutive Model," *International Journal of Solids and Structures,* vol. 46, no. 13, p. 2680–2692, 2009.

[16] C. Chisari, L. Macorini, C. Amadio and B. A. Izzuddin, " Identification of mesoscale model parameters for brick-masonry," *International Journal of Solids and Structures,* vol. 146, p. 224–240, 2018.

[17] E. Bertolesi, G. Milani and P. Lourenço, "Implementation and validation of a total displacement non-linear homogenization approach for in-plane loaded masonry," *Computers & Structures,* vol. 176, pp. 13-33, 2016.

[18] K. F. Abdulla, L. S. Cunningham and M. Gillie, "Simulating masonry wall behaviour using a simplified micro-model approach," *Engineering Structures,* vol. 151, p. 349–365, 2017.

[19] E. Reyes, J. C. Gálvez, M. J. Casati, D. A. Cendón, J. M. Sancho and J. Planas, "An embedded cohesive crack model for finite element analysis of brickwork masonry fracture," *Engineering Fracture Mechanics,* vol. 76, no. 12, p. 1930–1944, 2009.

[20] G. Milani, "3D Upper Bound Limit Analysis of Multi-Leaf Masonry Walls," *International Journal of Mechanical Sciences,* vol. 50, no. 4, p. 817–836, 2008.

[21] G. Milani, P. Lourenço and A. Tralli, "3D Homogenized Limit Analysis of Masonry Buildings Under Horizontal Loads," *Engineering Structures,* vol. 29, no. 11, p. 3134–3148, 2007 doi:10.1016/j.engstruct.2007.03.003.

[22] G. Milani, "Simple lower bound limit analysis homogenization model for in- and out-of-plane loaded masonry walls," *Construction & Building Materials,* vol. 25, p. 4426–4443, 2011.

[23] G. Milani and P. Lourenço, "A simplified homogenized limit analysis model for randomly assembled blocks out-of-plane loaded," *Computers & Structures,* vol. 88, p. 690–717, 2010.

[24] J. V. Lemos, "Discrete Element Modeling of Masonry Structures," *International Journal of Architectural Heritage,* vol. 1, no. 2, p. 190–213, 2007.

[25] H. Smoljanović, Ž. Nikolić and N. Živaljić, "A combined finite–discrete numerical model for analysis of masonry structures," *Engineering Fracture Mechanics,* vol. 136, p. 1–14, 2015.

[26] T. Bui, A. Limam, V. Sarhosis and M. Hjiaj., "Discrete Element Modelling of the in-Plane and Out-of-Plane Behaviour of Dry-Joint Masonry Wall Constructions," *Engineering Structures,* vol. 136, p. 277–294, 2017 doi:10.1016/j.engstruct.2017.01.020.

[27] S. Casolo and G. Milani, "Simplified out-of-plane modelling of three-leaf masonry walls accounting for the material texture," *Construction and Building Materials,* vol. 40, p. 330–351, 2013.

[28] D. Oliveira and P. Lourenço, "Implementation and validation of a constitutive model for the cyclic behaviour of interface elements," *Computers & Structures,* vol. 82, no. 17-19, p. 1451–1461, 2004.

[29] A. J. Aref and K. M. Dolatshahi, "A three-dimensional cyclic meso-scale numerical procedure for simulation of unreinforced masonry structures," *Computers & Structures,* vol. 120, p. 9–23, 2013.

[30] L. Gambarotta and S. Lagomarsino, "Damage models for the seismic response of brick masonry shear walls. Part I: the mortar joint model and its applications," *Earthquake engineering & structural dynamics,* vol. 26, no. 4, pp. 423-439, 1997.

[31] E. Sacco and J. Toti, "Interface Elements for the Analysis of Masonry Structures," *International Journal for Computational Methods in Engineering Science and Mechanics,* vol. 11, no. 6, p. 354–373, 2010.

[32] R. Serpieri, M. Albarella and E. Sacco, "A 3D Microstructured Cohesive–frictional Interface Model and Its Rational Calibration for the Analysis of Masonry Panels," *International Journal of Solids and Structures,* vol. 122–123, p. 110–127, 2017.

[33] D. Malomo, R. Pinho and A. Penna, "Using the applied element method for modelling calcium silicate brick masonry subjected to in-plane cyclic loading," *Earthquake Engineering & Structural Dynamics,* vol. 47, no. 7, p. 1610–1630, 2018.

[34] E. Minga, L. Macorini and B. A. Izzuddin, "A 3D mesoscale damage-plasticity approach for masonry structures under cyclic loading," *Meccanica,* 2017.

[35] A. D'Altri, S. de Miranda, G. Castellazzi and V. Sarhosis, "A 3D Detailed Micro-Model for the In-Plane and Out-Of-Plane Numerical Analysis of Masonry Panels," *Computers & Structures,* vol. 206, pp. 18-30, 2018.

[36] J. Lee and G. L. Fenves, "Plastic-Damage Model for Cyclic Loading of Concrete Structures," *Journal of Engineering Mechanics,* vol. 124, no. 8, p. 892–900, 1998.

[37] *Abaqus®. Theory manual, Version 6.17, 2017.*

[38] J. O. Hallquist, G. L. Goudreau and D. J. Benson, "Sliding interfaces with contact-impact in large-scale Lagrangian computations," *Computer Methods in Applied Mechanics and Engineering,* vol. 51, no. 1-3, p. 107–137, 1985.

[39] R. van der Pluijm, "Shear behaviour of bed joints," in *6th North American Masonry Conference, 6-9 June 1993*, Philadelphia, Pennysylvania, USA, 1993.

[40] M. Godio, I. Stefanou and K. Sab, "Effects of the dilatancy of joints and of the size of the building blocks on the mechanical behavior of masonry structures," *Meccanica,* 2017.

[41] R. van der Pluijm, H. Rutten and M. Ceelen, "Shear behaviour of bed joints," in *Proceedings of the Twelfth International Brick/Block Masonry Conference*, 2000.

[42] R. Weyler, J. Oliver, T. Sain and J. Cante, "On the Contact Domain Method: A Comparison of Penalty and Lagrange Multiplier Implementations," *Computer Methods in Applied Mechanics and Engineering,* vol. 205–208, p. 68–82, 2012.

[43] R. H. Atkinson, B. P. Amadei, S. Saeb and S. Sture, "Response of Masonry Bed Joints in Direct Shear," *Journal of Structural Engineering,* vol. 115, no. 9, p. 2276–2296, 1989.

[44] A. Mirmiran and M. Shahawy, "Dilation characteristics of confined concrete," *Mechanics of Cohesive-frictional Materials,* vol. 2, no. 3, p. 237–249, 1997.

[45] G. Milani, M. Valente and C. Alessandri, "The Narthex of the Church of the Nativity in Bethlehem: A Non-Linear Finite Element Approach to Predict the Structural Damage," *Computers & Structures,* 2017.

[46] G. Castellazzi, A. M. D'Altri, S. de Miranda and F. Ubertini, "An Innovative Numerical Modeling Strategy for the Structural Analysis of Historical Monumental Buildings," *Engineering Structures,* vol. 132, p. 229–248, 2017.

[47] J. Lubliner, J. Oliver, S. Oller and E. Oñate, "A Plastic-Damage Model for Concrete," *International Journal of Solids and Structures,* vol. 25, no. 3, p. 299–326, 1989.

[48] A. Formisano and A. Marzo, "Simplified and Refined Methods for Seismic Vulnerability Assessment and Retrofitting of an Italian Cultural Heritage Masonry Building," *Computers & Structures,* vol. 180, p. 13–26, 2017.

[49] F. Messali, R. Esposito, S. Jafari, G. Ravenshorst, P. Korswagen and J. Rots, "A multiscale experimental characterization of Dutch unreinforced masonry buildings," in *16th European Conference on Earthquake Engineering*, Thessaloniki, Greece, 2018.

[50] S. Jafari, J. G. Rots, R. Esposito and F. Messali, "Characterizing the Material Properties of Dutch Unreinforced Masonry," *Procedia Engineering,* vol. 193, pp. 250-257, 2017.

[51] F. Messali, G. E. R. Ravenshorst and J. Rots, "Large-scale testing program for the seismic characterization of Dutch masonry walls," in *16th World Conference on Earthquake*, Santiago, Chile, 2017.

[52] R. Esposito, K. Terwel, G. Ravenshorst, H. Shipper, F. Messali and J. Rots, "Cyclic pushover test on an unreinforced masonry structure reseambling a typical Dutch terraced house," in *16th World Conference on Earthquake*, Santiago, Chile, 2017.

[53] S. Jafari and R. Esposito, "Material tests for the characterisation of replicated calcium silicate brick masonry. Delft University of Technology. Report number C31B67WP1-9, version 01, 14 November 2016.," 2016.

[54] G. Ravenshorst, R. Esposito, R. Schipper, F. Messali, A. Tsouvalas, E.-M. Lourens and J. Rots, "Structural behaviour of a calcium silicate brick masonry assemblage: quasi-static cyclic pushover and dynamic identification test. Delft University of Technology, Department of Structural Engineering. Version 5, 21 October 2016," 2016.

[55] G. Castellazzi, A. M. D'Altri, S. de Miranda, A. Chiozzi and A. Tralli, "Numerical Insights on the Seismic Behavior of a Non-Isolated Historical Masonry Tower," *Bulletin of Earthquake Engineering,* vol. 16, no. 2, p. 933–961, 2018 doi.org/10.1007/s10518-017-0231-6.